J. Mech. Phys. Solids 173 (2023) 105219

Contents lists available at ScienceDirect

Journal of the Mechanics and Physics of Solids

journal homepage: www.elsevier.com/locate/jmps

Rate-dependent evolution of wrinkling films due to growth on semi-infinite planar viscoelastic substrates

Jan Zavodnik [a], Andrej Košmrlj [b,c,*], Miha Brojan [a,*]

[a] Faculty of Mechanical Engineering, University of Ljubljana, SI-1000 Ljubljana, Slovenia
[b] Department of Mechanical and Aerospace Engineering, Princeton University, Princeton, NJ 08544, USA
[c] Princeton Institute of Materials, Princeton University, Princeton, NJ 08544, USA

ARTICLE INFO

Keywords:
Thin film
Visco-hyperelasticity
Dissipation
Pattern evolution
Stability

ABSTRACT

A mechanistic understanding of morphogenesis in biology, the fabrication of advanced meta surfaces with specific functionalities and structures with enhanced energy dissipation often have in common that the combined effects of energy dissipation due to viscoelasticity and a loss of stability govern both their mechanical response and their final forms. In this paper we show that the interplay between viscoelasticity and multistability crucially influences the evolution of deformations in viscoelastic structures undergoing large deformations. The influence is studied on a prototypical system of a uniaxially growing film on a semi-infinite planar viscoelastic substrate, where it is shown that during the evolution of deformation the choice of multiple developing modes is greatly affected by this interplay. For the analysis of the underlying mechanics of the mode competition in the post-buckling regime, when the system undergoes large deformations, a 3D general finite-strain visco-hyperelastic theory is built. It includes kinematic and material nonlinearities in the film and in the substrate. For the case of ramp-loading time functions the phase space of the solutions is characterized and the evolution of a deformation pattern is analyzed. We find that the interaction between multistability and viscoelasticity greatly increases the evolution time of the system and that the growth rate and viscoelastic stress-relaxation rate influence the choice of the final equilibrium deformation state of the structure. This shows that viscoelastic structures can evolve into (meta)stable equilibrium states that are unattainable using purely elastic structures. The nonlinear problem is solved numerically with the use of the finite-element method. In parallel, we develop analytical solutions for a simplified problem that is based on Föppl–von Karman plate kinematics to describe the mechanics of the film and substrate that is modeled as a 2D linear-viscoelastic continuum. A remarkably good match between the analytical and the numerical results was obtained.

1. Introduction

The traditional analysis of stress–strain states in engineering systems is associated with the prediction and prevention of undesirable functional failure due to exceeding the stress or strain limits. Currently, many advanced applications are being developed on the basis of experimental and theoretical discoveries beyond these limits — in the nonlinear deformation regime, where a wealth of interesting physical mechanisms, such as jumps between deformation modes and various periodic patterns with favorable physical properties lead to innovative functional properties that can be used for actuation or control, e.g., in intelligent

* Correspondence to: Faculty of Mechanical Engineering, University of Ljubljana, SI-1000 Ljubljana, Slovenia.
E-mail addresses: andrej@princeton.edu (A. Košmrlj), miha.brojan@fs.uni-lj.si (M. Brojan).

https://doi.org/10.1016/j.jmps.2023.105219
Received 21 October 2022; Received in revised form 12 January 2023; Accepted 13 January 2023
Available online 24 January 2023

adhesive systems (Lin et al., 2008), for super-hydrophilicity/hydrophobicity (Sabbah et al., 2016), soft robotics (Truby et al., 2018), prosthetics (Kawasaki and Mouri, 2019), measuring material properties (Pocivavsek et al., 2008) and, e.g., gaining mechanistic descriptions of morphogenesis in biology (Goodwin et al., 2019; Goriely and Ben Amar, 2007; Balbi et al., 2015; Rauzi et al., 2008; Yan et al., 2019).

A lot of these systems were developed on soft synthetic and natural polymers. These materials generally exhibit time-dependent (viscous) internal energy dissipation, irreversible deformations, a phase shift between loads and deformations, a nonlinear relationship between stresses and strains, and strain rates on multiple time scales. In conventional static structural engineering with natural and synthetic polymers, such phenomena are often neglected and only the immediate response (in the time limit $t \to 0$) is taken into account (sometimes also the equilibrium response limit as $t \to \infty$). This is acceptable in a static analysis when deformations are small, the material's behavior is linear, the load–deformation relation is unique and the viscoelastic stress relaxation time is long. However, the load–deformation relation might not be unique and the structure could exhibit multiple stable equilibrium states in the presence of either geometric or material nonlinearities. In this case and in the presence of viscous effects, the consequent transient nature of the problem can also influence the final equilibrium state and therefore the temporal component must be accounted for.

The stability of purely elastic structures due to geometric/material nonlinearities has been thoroughly studied and discussed for many isolated flexible structures (beams, plates and shells) or when those adhered to soft substrates, see, e.g., Allen (1969), Hutchinson (2013), Cao and Hutchinson (2012), Chen and Hutchinson (2004), Audoly and Boudaoud (2008) and Huang et al. (2005). Viscoelasticity has also been well studied, mostly in the context of rheology, see, e.g., Christensen (1982a), Budday et al. (2017), Harris et al. (2012), Berthier and Kurchan (2013) and Matoz-Fernandez et al. (2017). On the other hand, literature on the coupling of both physical aspects and a consideration of the transient part of the deformation's evolution is surprisingly scarce. Most studies have considered only the elastic limits of viscoelasticity for a mechanistic explanation of biological morphogenesis (Tallinen et al., 2016; de Rooij and Kuhl, 2017; Budday et al., 2014; Shyer et al., 2013; Balbi et al., 2015; Goodwin et al., 2019), often considering theories of growth mechanics (Ben Amar and Goriely, 2005; Goriely and Ben Amar, 2007). However, there are some studies showing that dissipative viscoelastic effects, which are often disregarded, can impact significantly on the evolution of deformation. As it turns out, flexible-structure, soft-substrate composites are ideal for a fundamental exploration of the interplay between multi-stability and viscoelasticity, because the energy of the system is released, both through local deformation (in terms of the formation of (quasi-)periodic wrinkling patterns) of the film and through viscoelastic relaxation of the stresses in the substrate, while at the same time being relatively simple. Huang (2002, 2005), Im and Huang (2005, 2008), Brau et al. (2013) and McRae et al. (2021) were the first to analyze the interplay between the stability of periodic deformation patterns due to geometric nonlinearity and the viscoelasticity in thin elastic films deposited on viscoelastic substrates under compression due to confined growth, swelling, temperature or external forces. Their studies focused on the evolution of viscoelastic deformation at the onset of the elastic wrinkling limits (immediate response limit as $t \to 0$ and equilibrium response limit as $t \to \infty$) for the step loading of a film with residual compressive membrane stresses. Two qualitatively different wrinkling responses were identified: (i) a kinetic wrinkling response, where the stresses are insufficient to cause instant dynamic wrinkling, but sufficient to cause slow the kinetic deformation pattern development from the undeformed to the final equilibrium wrinkled state, and (ii) a dynamic wrinkling response where the stresses are sufficient to induce instant dynamic meta-stable wrinkle deformation, which then evolves towards the final stable equilibrium deformation. Unfortunately, due to the linearization (Huang, 2005) and the assumption of linear viscoelasticity of the substrate (Im and Huang, 2005), the nonlinear effects, such as the competition between the deformation modes during pattern evolution, the transitions between the meta-stable deformation states and the establishment of the final locally stable and frozen equilibrium deformation mode, were not observed. Recently, Matoz-Fernandez et al. (2020) investigated the nonlinear regime of wrinkling for an elastic film, subjected to active remodeling without a substrate. They discovered that such structures can exhibit deformation patterns unattainable with purely elastic structures, yet the mechanisms of such deformations were not thoroughly explained.

In this paper we study the evolution of the deformation of a flat elastic film that grows uniaxially on a semi-infinite planar viscoelastic substrate. The response of such a structure is largely nonlinear due to the nonlinear connection between the membrane strains and the out-of-plane wrinkling displacements and due to the moderately large strains in the substrate. For an accurate description of the response, we combine a visco-hyperelastic (VH) finite strain and growth theory through the multiplicative decomposition of the deformation gradients. With this coupling it is possible to model general 2D viscoelastic structures undergoing growth, e.g., by tissue growth, hydrogel swelling, or polymerization. The theory is also applicable to spatial (3D) structures.

With our model we go beyond linear analysis and explore the full transient and equilibrium evolution of deformation, analyze the competition between the developing deformation modes as well as its underlying mechanics for different loading functions of imposed uniaxial growth strain in the direction of the film's mid-surface. We explore the occurrence of metastable deformation states, phase shifting between load and deformation and whether the deformation's evolution time scale increases due to the interplay between viscoelasticity and multistability. We analyze whether this interplay can result in seemingly non-equilibrium "frozen" final deformation patterns and search for the final equilibrium deformation patterns that might not be attainable with purely elastic structures. To solve the fully nonlinear system of equations of the VH theory, we use triangular, solid 2D finite elements of the third degree implemented in the FEniCS FE computational framework (Logg et al., 2011; Alnæs et al., 2015). For solving the very nonlinear system of equations we use the Newton–Raphson method and dynamic relaxation numerical methods (Joldes et al., 2011b), which allow us to observe the very nonlinear behavior due to the loss of stability and the intense changes in loading. Due to the vastness of the parametric space that we need to analyze, we develop a toy model with which we are able to chart and characterize the behavior of the analyzed system in the regime of moderate deformations much more easily and rapidly. The developed toy model is inspired by the work of Huang (2005), who analyzed the development of wrinkles of an elastic film on a viscoelastic substrate subjected to step-function growth in the elastic film. Similar to Huang's model, we considered reduced kinematics, based on the

Föppl–von Karman (FvK) plate assumptions for the modeling of the elastic film. We expand his model by considering the influence of the viscoelastic substrate in a more accurate way, similar to what Audoly and Boudaoud (2008) did for the elastic substrate, and do not disregard the nonlinear terms in the FvK theory of the film. An arbitrary time function of loading can be applied in our model. We used a ramp time function of loading, which can be reduced to a step function, when the constrained growth strain rate is infinite. Furthermore, to check the validity of our toy model we also linearized our theory and used step-function loading to obtain qualitatively similar results as Huang (2005).

The rest of this paper is organized as follows: In Section 2 we present our general finite-strain continuum visco-hyperelastic theory for modeling the deformations of arbitrary 3D viscoelastic structures and growth strain. We introduce the time shape functions of growth strain, the characteristic stress response of viscoelastic materials and the toy model for a simplified characterization of the different types of deformation responses of the structure. In Section 3 we analyze the different types of deformation-pattern evolution due to the different growth functions (as a function of time) and the different choice of material parameters. We observe the transient deformation-pattern evolution and especially the competition between deformation modes and their influence on the final equilibrium deformation patterns. In Section 4 we summarize our findings and provide perspectives for future extensions of the current work.

2. Theory

Here, we present a finite-deformation visco-hyperelastic (VH) theory that takes into account geometric nonlinearities by considering the finite-deformation kinematics and the material nonlinearity through the application of the neo-Hookean material law. In conjunction with our toy model, which is also presented below, here we use our general VH theory, which is otherwise applicable to any 3D structure, to study a 2D plane-strain system comprising a uniaxially growing elastic film on a semi-infinite viscoelastic substrate and analyze the coupling between the viscoelasticity and the multi-stability, which results from the geometric and material nonlinearities.

2.1. Finite-deformation visco-hyperelastic theory

(Kinematics) A continuous body in the initial configuration $\mathcal{G}_0$, parametrized with $\boldsymbol{X}$ transforms into a current configuration $\mathcal{G}$, parametrized by $\boldsymbol{x}$, due to the deformation χ, i.e.

$$\chi : \mathcal{G}_0 \to \chi(\mathcal{G}_0) =: \mathcal{G} \quad \text{and} \quad \chi : \boldsymbol{X} \mapsto \chi(\boldsymbol{X}) =: \boldsymbol{x}. \tag{1}$$

The displacement $\boldsymbol{u}$ between the initial and the current configuration is defined as $\boldsymbol{u} := \boldsymbol{x} - \boldsymbol{X}$. Therefore, we can write the deformation gradient as

$$\mathbf{F} = \frac{\partial \boldsymbol{x}}{\partial \boldsymbol{X}} = \nabla \boldsymbol{x} = \mathbf{I} + \nabla \boldsymbol{u}. \tag{2}$$

The growth of the structure is taken into account through a multiplicative decomposition of the deformation gradient $\mathbf{F}$, which is decomposed into the deformation gradient of the growth $\mathbf{F}_g$ and the deformation gradient of the visco-elastic part $\mathbf{F}_c$, such that $\mathbf{F} = \mathbf{F}_c\mathbf{F}_g$, see, e.g., Ben Amar and Goriely (2005), Yavari (2010), Hoger (1997) and Lubarda and Hoger (2002). Furthermore, using the viscoelastic constitutive material law (Hrapko et al., 2006; Bilston et al., 2001; Prevost et al., 2011; Reese and Govindjee, 1998) schematically represented in Fig. 1a, we propose that the constitutive part of the deformation gradient $\mathbf{F}_c$ should also be represented in terms of the equilibrium elastic part of the deformation $\mathbf{F}_c = \mathbf{F}_{eq,e}$, or be decomposed into a non-equilibrium elastic (transient) and viscous deformation gradient, such that $\mathbf{F}_c = \mathbf{F}_v\mathbf{F}_{neq,e}$. Here, $\mathbf{F}_{eq,e}$ is the purely elastic (equilibrium, non-transient) deformation gradient part, and $\mathbf{F}_{neq,e}$ is the elastic part of the (non-equilibrium, transient) deformation gradient. Here, we use standard notation for the $\mathbf{F}_{eq,e}$ and $\mathbf{F}_{neq,e}$ parts of the deformation gradient, which are the equilibrium and non-equilibrium parts of the deformation in the case that the structure is loaded with a step-time loading function (Reese and Govindjee, 1998; Prevost et al., 2011; Carniel and Fancello, 2017). Finally, the deformation gradient can be decomposed into $\mathbf{F} = \mathbf{F}_v\mathbf{F}_{neq,e}\mathbf{F}_g$ or $\mathbf{F} = \mathbf{F}_{eq,e}\mathbf{F}_g$, as schematically represented in Fig. 1(b).

(Constitutive material model) We assume a visco-hyperelastic (VH) material constitutive model that includes viscoelastic energy dissipation and can be expressed with the Rayleigh potential $\mathbb{P}$. In general, we would need to solve dynamic equilibrium equations due to the viscoelasticity, which introduces time dependent variables into the system; however, with the use of the Rayleigh potential, which in our case consists of elastic and viscous parts, we are able to translate the problem into an energy-flow optimization problem (Carniel and Fancello, 2017). The Rayleigh potential comprises the static equilibrium free energy rate per unit of reference volume $\dot{\Psi}_{eq}$, the static non-equilibrium free energy per unit of reference volume $\dot{\Psi}_{neq}$ and the viscous dissipation per unit of reference volume Φ. The Rayleigh potential of the whole system is therefore

$$\mathcal{P} = \int_{\Omega} \mathbb{P}\, d\Omega = \int_{\Omega_0} \left(\dot{\Psi}_{eq} + \dot{\Psi}_{neq} + \Phi\right) J_g\, d\Omega_0 \tag{3}$$

where $J_g = \det(\mathbf{F}_g)$ is the determinant of the growth-deformation gradient, which accounts for the change of volume due to the growth (Ben Amar and Goriely, 2005). The hyperelastic material law that we use is a neo-Hookean material, which is thermodynamically consistent (Ogden, 2013), as opposed to the most commonly used St. Venant-Kirchhoff (sometimes referred

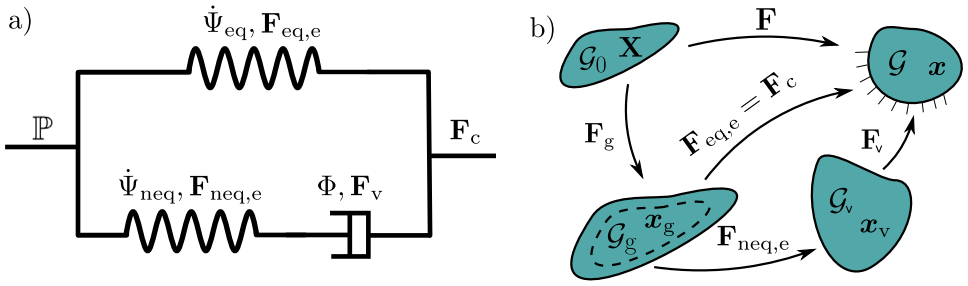

Fig. 1. Constitutive modeling. (a) A schematic representation of the standard linear solid constitutive visco-hyperelastic model (Hrapko et al., 2006; Prevost et al., 2011; Bilston et al., 2001; Reese and Govindjee, 1998; Carniel and Fancello, 2017). The Rayleigh potential $\mathbb{P}$ (energy rate per unit initial volume) is decomposed into the equilibrium (permanent) elastic free energy rate $\dot{\Psi}_{\mathrm{eq}}$, non-equilibrium (transient) elastic free energy rate $\dot{\Psi}_{\mathrm{neq}}$ and viscous dissipation Φ. The equilibrium elastic free energy Ψ_{eq} is constant when the system reaches static equilibrium, while the non-equilibrium elastic free energy Ψ_{neq} vanishes at static equilibrium. (b) (Multiplicative) decomposition of the deformation gradient $\mathbf{F}$ into the imposed growth deformation gradient $\mathbf{F}_{\mathrm{g}}$ and the equilibrium elastic deformation gradient $\mathbf{F}_{\mathrm{eq,e}}$. Note that $\mathbf{F}_{\mathrm{eq,e}}$ is equal to the constitutive deformation gradient $\mathbf{F}_{\mathrm{c}}$, which can be further decomposed into the non-equilibrium (transient) dissipative deformation gradient $\mathbf{F}_{\mathrm{v}}$ and the non-equilibrium (transient) elastic deformation gradient $\mathbf{F}_{\mathrm{neq,e}}$.

to as generalized Hooke's) material law, which exhibits nonphysical behavior in a material under large compressive pressures. The strain–energy density function $\Psi_{\alpha}^{\mathrm{neo}}$ for a compressible neo-Hookean material is

$$\Psi_{\alpha}^{\mathrm{neo}} = \frac{\mu_{\alpha}}{2}\left(\mathrm{tr}\left(\mathbf{C}_{\alpha,\mathrm{e}}\right) - 3 - 2\ln J_{\alpha,\mathrm{e}}\right) + \frac{\Lambda_{\alpha}}{2}\left(\ln J_{\alpha,\mathrm{e}}\right)^2, \tag{4}$$

where $\mathbf{C}_{\alpha,\mathrm{e}} = \mathbf{F}_{\alpha,\mathrm{e}}^{\mathrm{T}}\mathbf{F}_{\alpha,\mathrm{e}}$ and $J_{\alpha,\mathrm{e}} = \det\left(\mathbf{F}_{\alpha,\mathrm{e}}\right)$ are the right Cauchy–Green strain tensors, deformation gradients and determinants of the deformation gradient, respectively. The material parameters are the first $\Lambda_{\alpha} = E_{\alpha}\nu_{\alpha}/((1+\nu_{\alpha})(1-2\nu_{\alpha}))$ and second $\mu_{\alpha} = E_{\alpha}/(2(1+\nu_{\alpha}))$ Lame parameters, while E_{α} and ν_{α} are the Young's modulus and Poisson's ratio. For the case of the equilibrium viscoelastic part $\alpha = \mathrm{eq}$ and for the non-equilibrium viscoelastic part $\alpha = \mathrm{neq}$. A simple dissipation pseudo-potential Φ according to Hrapko et al. (2006), Prevost et al. (2011) and Bilston et al. (2001) can be written as a function of $\mathbf{l}_{\mathrm{v}}$,

$$\Phi = \eta\, \mathbf{l}_{\mathrm{v}} : \mathbf{l}_{\mathrm{v}}, \tag{5}$$

where η is the dynamic viscosity, which corresponds to the product of the non-equilibrium shear modulus and the viscoelastic stress-relaxation time $\eta = \mu_{\mathrm{neq}}\tau$, and $\mathbf{l}_{\mathrm{v}} = 1/2\left(\mathbf{d}_{\mathrm{v}} + \mathbf{d}_{\mathrm{v}}^{\mathrm{T}}\right)$ is a symmetrical part of the viscous velocity gradient. The viscous velocity gradient is defined as $\mathbf{d}_{\mathrm{v}} := \partial\dot{\boldsymbol{x}}_{\mathrm{v}}/\partial\boldsymbol{x} = \left(\partial\dot{\boldsymbol{x}}_{\mathrm{v}}/\partial\boldsymbol{x}_{\mathrm{v}}\right)\left(\partial\boldsymbol{x}_{\mathrm{v}}/\partial\boldsymbol{x}\right) = \dot{\mathbf{F}}_{\mathrm{v}}\mathbf{F}_{\mathrm{v}}^{-1}$, where $\dot{\boldsymbol{x}}_{\mathrm{v}}$ is the velocity of the viscous intermediate configuration and $\boldsymbol{x}_{\mathrm{v}}$ is the position vector in the intermediate configuration of the system, see Fig. 1(b). Multiplying the rate of the viscous left Cauchy green tensor $\dot{\mathbf{C}}_{\mathrm{v}} = \mathbf{F}_{\mathrm{v}}^{\mathrm{T}}\dot{\mathbf{F}}_{\mathrm{v}} + \dot{\mathbf{F}}_{\mathrm{v}}^{\mathrm{T}}\mathbf{F}_{\mathrm{v}}$ with $\mathbf{F}_{\mathrm{v}}^{-\mathrm{T}}$ from the left and $\mathbf{F}_{\mathrm{v}}^{-1}$ from the right yields $\dot{\mathbf{C}}_{\mathrm{v}}\mathbf{C}_{\mathrm{v}}^{-1} = \dot{\mathbf{F}}_{\mathrm{v}}\mathbf{F}_{\mathrm{v}}^{-1} + \left(\dot{\mathbf{F}}_{\mathrm{v}}\mathbf{F}_{\mathrm{v}}^{-1}\right)^{\mathrm{T}}$, which can be substituted into the symmetrical part of the velocity gradient to obtain $\mathbf{l}_{\mathrm{v}} = \dot{\mathbf{C}}_{\mathrm{v}}\mathbf{C}_{\mathrm{v}}^{-1}/2$ in terms of the viscous left Cauchy–Green strain tensor (Hrapko et al., 2006; Prevost et al., 2011; Bilston et al., 2001).

(Whole model) Using the kinematic relations $\mathbf{F}_{\mathrm{eq,e}} = \mathbf{F}_{\mathrm{g}}^{-1}\mathbf{F}$ and $\mathbf{F}_{\mathrm{neq,e}} = \mathbf{F}_{\mathrm{g}}^{-1}\mathbf{F}\mathbf{F}_{\mathrm{v}}^{-1}$ we can express the Rayleigh potential as a function of displacements $\boldsymbol{u}$ and velocities $\dot{\boldsymbol{u}}$ (through the right Cauchy–Green strain tensor $\mathbf{C} = \mathbf{F}\mathbf{F}^{\mathrm{T}}$, where the deformation gradient $\mathbf{F} = \nabla\boldsymbol{u} + \mathbf{I}$ and its rate $\dot{\mathbf{F}} = \nabla\dot{\boldsymbol{u}}$), internal variables of the viscous left Cauchy–Green tensor $\mathbf{C}_{\mathrm{v}}$ and its rate $\dot{\mathbf{C}}_{\mathrm{v}}$, then

$$\mathcal{P}\left(\boldsymbol{u}, \mathbf{C}_{\mathrm{v}}, \dot{\mathbf{C}}_{\mathrm{v}}\right) = \int_{\Omega_0}\left(\dot{\Psi}_{\mathrm{eq}}(\mathbf{C}_{\mathrm{g}}^{-1}\mathbf{C}(\boldsymbol{u})) + \dot{\Psi}_{\mathrm{neq}}(\mathbf{C}_{\mathrm{g}}^{-1}\mathbf{C}(\boldsymbol{u})\mathbf{C}_{\mathrm{v}}^{-1}) + \Phi(\dot{\mathbf{C}}_{\mathrm{v}}\mathbf{C}_{\mathrm{v}}^{-1})\right) J_g\, d\Omega_0. \tag{6}$$

This can be rewritten using the chain rule as

$$\mathcal{P}\left(\boldsymbol{u}, \mathbf{C}_{\mathrm{v}}, \dot{\mathbf{C}}_{\mathrm{v}}\right) = \int_{\Omega_0}\left(\frac{\partial\Psi_{\mathrm{eq}}(\mathbf{C}_{\mathrm{g}}^{-1}\mathbf{C})}{\partial\mathbf{C}} : \dot{\mathbf{C}} + \frac{\partial\Psi_{\mathrm{neq}}(\mathbf{C}_{\mathrm{g}}^{-1}\mathbf{C}\mathbf{C}_{\mathrm{v}}^{-1})}{\partial\mathbf{C}} : \dot{\mathbf{C}} + \frac{\partial\Psi_{\mathrm{neq}}(\mathbf{C}_{\mathrm{g}}^{-1}\mathbf{C}\mathbf{C}_{\mathrm{v}}^{-1})}{\partial\mathbf{C}_{\mathrm{v}}} : \dot{\mathbf{C}}_{\mathrm{v}} + \Phi(\dot{\mathbf{C}}_{\mathrm{v}}\mathbf{C}_{\mathrm{v}}^{-1})\right) J_g\, d\Omega_0. \tag{7}$$

To compute $\boldsymbol{u}$ and $\mathbf{C}_{\mathrm{v}}$ we seek an extremum of the Rayleigh potential with the use of calculus of variation

$$\begin{aligned}\delta\mathcal{P}_{\dot{\boldsymbol{u}}}\left(\boldsymbol{u}, \mathbf{C}_{\mathrm{v}}, \dot{\mathbf{C}}_{\mathrm{v}}\right) &= 0,\\ \delta\mathcal{P}_{\dot{\mathbf{C}}_{\mathrm{v}}}\left(\boldsymbol{u}, \mathbf{C}_{\mathrm{v}}, \dot{\mathbf{C}}_{\mathrm{v}}\right) &= 0.\end{aligned} \tag{8}$$

Although we are using Eq. (8) to solve the system, we can show that the variation with respect to the global displacements rate $\dot{\boldsymbol{u}}$ yields a weak form of Cauchy stress-equilibrium equation on the deformed geometry $\nabla_{\boldsymbol{x}}\cdot\boldsymbol{\sigma} = \mathbf{0}$:

$$\begin{aligned}\delta\mathcal{P}_{\dot{\boldsymbol{u}}} &= \int_{\Omega_0}\left(\frac{\partial\Psi_{\mathrm{eq}}}{\partial\mathbf{F}_{\mathrm{eq,e}}}\frac{\partial\mathbf{F}_{\mathrm{eq,e}}}{\partial\mathbf{F}} + \frac{\partial\Psi_{\mathrm{neq}}}{\partial\mathbf{F}_{\mathrm{neq,e}}}\frac{\partial\mathbf{F}_{\mathrm{neq,e}}}{\partial\mathbf{F}}\right) : \frac{\partial\delta\dot{\boldsymbol{u}}}{\partial\boldsymbol{X}} J_{\mathrm{g}} d\Omega_0\\ &= \int_{\Omega_0}\left(\mathbf{P}_{\mathrm{eq,g}}\mathbf{F}_{\mathrm{g}}^{-1} + \mathbf{P}_{\mathrm{neq,g}}\mathbf{F}_{\mathrm{g}}^{-1}\mathbf{F}_{\mathrm{v}}^{-1}\right) : \frac{\partial\delta\dot{\boldsymbol{u}}}{\partial\boldsymbol{X}} J_{\mathrm{g}} d\Omega_0\\ &= \int_{\Omega}\left(\left(\boldsymbol{\sigma}_{\mathrm{eq,g}} + \boldsymbol{\sigma}_{\mathrm{neq,g}}\right)\mathbf{F}^{-1}\right) : \frac{\partial\delta\dot{\boldsymbol{u}}}{\partial\boldsymbol{X}} d\Omega = \int_{\Omega}\frac{\partial\boldsymbol{\sigma}}{\partial\boldsymbol{x}}\cdot\delta\dot{\boldsymbol{u}} d\Omega = 0\end{aligned} \tag{9}$$

Here, $\boldsymbol{\sigma}_{\mathrm{eq,g}}$ and $\boldsymbol{\sigma}_{\mathrm{neq,g}}$ are the Cauchy stress tensors of the equilibrium and non-equilibrium branches, respectively, and $\mathbf{P}_{\mathrm{eq,g}}$ and $\mathbf{P}_{\mathrm{neq,g}}$ are the first Piola–Kirchhoff stress tensors of the equilibrium and non-equilibrium branches, respectively. The variation with respect to $\mathbf{C}_{\mathrm{v}}$ yields an internal constitutive equation

$$\delta\mathcal{P}_{\dot{\mathbf{C}}_{\mathrm{v}}} = \int_{\Omega_0} \left(\frac{\partial \Psi_{\mathrm{neq}}}{\partial \mathbf{F}_{\mathrm{neq,e}}} \frac{\partial \mathbf{F}_{\mathrm{neq,e}}}{\partial \mathbf{F}_{\mathrm{v}}} \frac{\partial \mathbf{F}_{\mathrm{v}}}{\partial \mathbf{C}_{\mathrm{v}}} + \frac{\partial \boldsymbol{\Phi}}{\partial \mathbf{l}_{\mathrm{v}}} \frac{\partial \mathbf{l}_{\mathrm{v}}}{\partial \dot{\mathbf{C}}_{\mathrm{v}}} \right) : \delta\dot{\mathbf{C}}_{\mathrm{v}} J_{\mathrm{g}} d\Omega_0 = \int_{\Omega_0} \frac{1}{2} \left(\left(-\boldsymbol{\sigma}_{\mathrm{neq,e}} + \boldsymbol{\sigma}_{\mathrm{v}} \right) \mathbf{C}_{\mathrm{v}}^{-1} \right) : \delta\dot{\mathbf{C}}_{\mathrm{v}} J_{\mathrm{g}} d\Omega_0 = 0 \tag{10}$$

(also called the internal variables evolution equation) that requires equality between the true stresses of the non-equilibrium elastic part of the constitutive material model (non-equilibrium spring in the analogy in Fig. 1a) and that of the viscous part $\boldsymbol{\sigma}_{\mathrm{neq,e}} = \boldsymbol{\sigma}_{\mathrm{v}}$ (dashpot in the analogy in Fig. 1a).

2.2. Time-dependent loading and viscoelastic stress relaxation

The response of a viscoelastic structure greatly depends on the type of load (imposed stress/strain or a combination of both) and on the loading mode (its shape, rate, etc.). To characterize its response we choose to load the film with a horizontal growth strain, which loads the viscoelastic substrate with a combination of imposed stress and strain. We choose the time-shape functions of a ramp, a limited ramp and a step function, defined with the following expression

$$\varepsilon_{\mathrm{g}}(t; \dot{\varepsilon}_{\mathrm{g}}, \bar{\varepsilon}_{\mathrm{g}}) = \begin{cases} 0, & 0 \le t < t_0, \\ \dot{\varepsilon}_{\mathrm{g}}(t - t_0), & t_0 \le t < \bar{t}, \\ \bar{\varepsilon}_{\mathrm{g}}, & t \ge \bar{t}, \end{cases} \tag{11}$$

as shown in Fig. 2a, where $\bar{t} = \bar{\varepsilon}_{\mathrm{g}}/\dot{\varepsilon}_{\mathrm{g}} + t_0$. The imposed horizontal growth strain in our VH theory enters our 2D system through the growth-deformation gradient

$$\mathbf{F}_{\mathrm{g}}(t) = \begin{pmatrix} 1 + \varepsilon_{\mathrm{g}}(t) & 0 \\ 0 & 1 \end{pmatrix}. \tag{12}$$

The nearly incompressible viscoelastic substrate is in our case subjected to a Robin-type boundary load (analogous to loading through an elastic spring) and is a function of time. However, for the sake of understanding its response to loading we can consider a case where the shear strain $\bar{\varepsilon}$ is imposed on the substrate in the form of a time step function. This is also called the viscoelastic stress-relaxation test. Initially, when the structure is loaded and the dashpot has not had time to deform, the strain load instantly causes an immediate stress response $\sigma_{\mathrm{s}}^0 := \lim_{t \to 0} \sigma_{\mathrm{s}}(t)$ from both branches (the equilibrium and non-equilibrium branches) of the spring–dashpot analogy, schematically depicted in Fig. 1a. Then, with time, the dashpot in the non-equilibrium branch starts to deform and relaxes the elastic spring in series with it, which causes a lowering in the stress response of the branch. Therefore, the total stress response decreases with time $\sigma_{\mathrm{s}}(t)$, which is called viscoelastic stress relaxation. Finally, when the non-equilibrium dashpot–spring branch relaxes fully, only the elastic equilibrium stress response due to the elastic equilibrium branch remains $\sigma_{\mathrm{s}}^{\infty} := \lim_{t \to \infty} \sigma_{\mathrm{s}}(t)$.

Therefore, for the case of the time-step loading with strain, we can define effective shear moduli of the immediate, transitional and equilibrium response as $\mu_{\mathrm{s}}^0 = \sigma_{\mathrm{s}}^0/\bar{\varepsilon}$, $\mu_{\mathrm{s}}(t) = \sigma_{\mathrm{s}}(t)/\bar{\varepsilon}$ and $\mu_{\mathrm{s}}^{\infty} = \sigma_{\mathrm{s}}^{\infty}/\bar{\varepsilon}$, respectively, where $\bar{\varepsilon}$ is the prescribed shear strain in the substrate and σ_{s} is the shear stress in the substrate. The immediate and the final response shear moduli can also be calculated from the responses of both springs in the spring–dashpot analogy (see Fig. 1(*a*)) as $\mu^0 = \mu_{\mathrm{eq}} + \mu_{\mathrm{neq}}$ and $\mu^{\infty} = \mu_{\mathrm{neq}}$, respectively. Even though our loading case is more complex due to the load being applied through the film, which is a combination of time-dependent strain and stress loading, the above effective shear moduli can help us to understand the viscoelastic behavior of the system due to the viscoelastic lowering of the effective stiffness.

In parallel with our VH finite-strain model we developed a relatively simple, weakly nonlinear toy model, which will be discussed in the section below. It considers moderately large displacements and can therefore describe the early post-buckling behavior of the system relatively accurately and allows us a rapid combining of the parametric space. It is also able to capture the competition between the deformation modes, the response of the system when subjected to an arbitrary time-dependent loading and considers the effective stiffness of the substrate, which is derived from the assumption that the substrate is a continuum rather than using other assumptions (e.g., a Winkler-type foundation). We mainly analyze the ramp-time function of loading. In the limit, as the constrained growth strain rate goes to infinity, a step loading is obtained, and by linearization of our toy model we obtain qualitatively similar results as in the seminal paper by Huang (2005).

2.3. Toy model

We build our toy model on the Föppl–von Karman (FvK) plate assumptions (Lifshitz et al., 1986; Timoshenko and Gere, 2012) that consider a weakly nonlinear relationship between the plate's membrane strains and its out-of-plane displacements. This plate model is used to describe the mechanics of the elastic film attached on top of an infinitely thick, linearly viscoelastic continuum. In addition to Im and Huang (2005), Huang (2005), we describe the substrate more accurately and model the linearly elastic continuum based on the work by Audoly and Boudaoud (2008), but with the use of viscoelastic material properties from Christensen (1982b), see Fig. 3. In contrast to our VH theory, our toy model does not include nonlinearities in the substrate. The mid-surface of the plate and the top boundary of the viscoelastic substrate are connected such that the normal stress and displacements are continuous, while the tangential traction is assumed to be zero. As a consequence, the horizontal displacements u of the mid-surface can only be

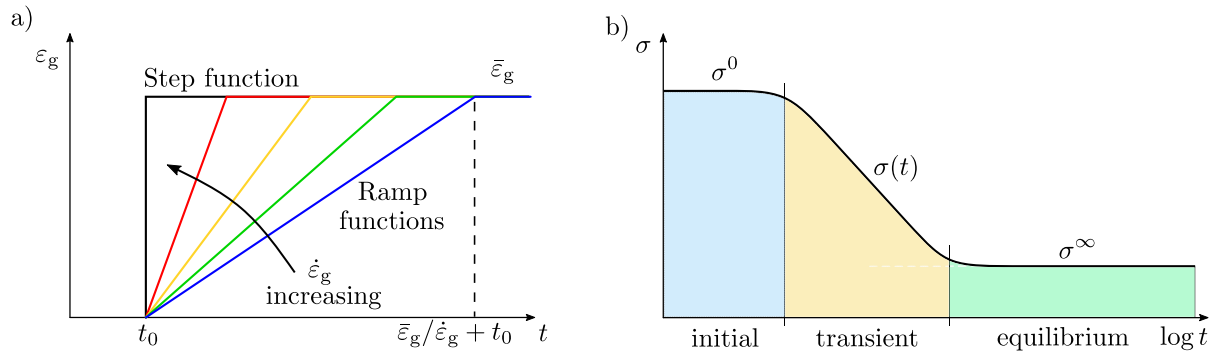

Fig. 2. Time-dependent loading conditions and limit material properties. (a) Continuous (linearly increasing) growth strain functions ε_g as limited ramp functions of time t with different strain rates $\dot{\varepsilon}_g$. In the limit, as $\dot{\varepsilon}_g \to \infty$, the growth function becomes a step function, which corresponds to instantaneous load application at time t_0. (b) Viscoelastic stress $\sigma(t)$ as a function of time t for step loading. The stress response $\sigma(t)$ consists of three phases: initial stress $\sigma^0 := \lim_{t\to 0}\sigma(t)$, transitional stress $\sigma(t)$ and equilibrium stress $\sigma^\infty := \lim_{t\to\infty}\sigma(t)$.

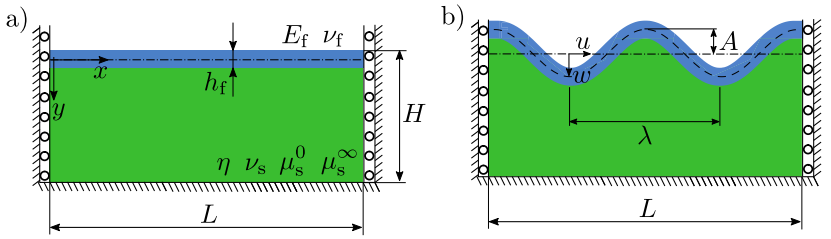

Fig. 3. Toy model of an elastic film adhered to a viscoelastic 2D solid substrate modeled under a plane-strain assumption. (a) Reference configuration. The symbols E_f, ν_f, h_f denote the Young's modulus, Poisson's ratio and thickness of the film, respectively, while ν_s is Poisson's ratio, η is the coefficient of dynamic viscosity, μ_s^0 and μ_s^∞ are the immediate and equilibrium shear moduli of the substrate. The length and height of the structure are denoted by L and H, respectively. The structure is fixed at the bottom and locked for horizontal displacements on the side edges. (b) The current configuration features a surface-wrinkling pattern with a characteristic wavelength λ and amplitude A. Displacements of the film's centroid in the x and y directions are denoted by u and w, respectively.

computed through balancing the horizontal membrane forces in the plate, which is shown to be a good approximation, see Audoly and Boudaoud (2008). To load the film we use an additive decomposition of the mid-surface in-plane strain $\varepsilon = \varepsilon_g + \varepsilon_e$, where ε is the total membrane strain of the film, ε_e is the elastic part of the total membrane strain and ε_g is the growth strain.

We assume that after the critical normal stress due to confined growth is reached, the film starts to form a periodic wrinkling pattern. To describe its shape in terms of vertical displacements we, in contrast to Huang (2005) where only one harmonic function was used, employ a sum of harmonic functions $w(x) = \sum_{n=1}^{\infty} A_n(t)\cos(k_n x)$ to describe the displacement of the mid-surface of the film. Here, $A_n(t)$ describes the amplitudes of the deformation modes and the wave numbers $k_n = 2\pi n/L = 2\pi/\lambda$ describe the wavelength of the deformation mode, which can be expressed in terms of the number of wrinkles n of the deformation mode. Note that this ansatz automatically satisfies the boundary conditions presented in Fig. 3.

To find the wrinkling pattern we seek the amplitude spectrum $A_n(t)$ that maximizes the total energy dissipation of the film and the substrate. The total strain energy of the film is equal to the sum of the bending- and membrane-strain energies, where the curvature and membrane strain are $\kappa_{\text{elastic}} = w''(x)$ and $\varepsilon_{\text{elastic}} = u'(x) + w'(x)^2/2 - \varepsilon_g$, therefore:

$$\mathcal{E}_f = \frac{1}{L}\int_L \left(\frac{1}{2}Dw''(x)^2 + \frac{1}{2}C\left(u'(x) + \frac{1}{2}w'(x)^2 - \varepsilon_g\right)^2\right)dx. \tag{13}$$

Here, $D = E_f h_f^3/(12(1-\nu_f^2))$ is the bending rigidity and $C = E_f h_f/(1-\nu_f^2)$ is the membrane rigidity of the film. The subscript f designates that the energy corresponds to that of the film.

At this point we assume that the lateral displacement $u(x)$ only causes membrane forces in the film and does not affect the substrate, which was shown to be a good approximation for a soft substrate in Audoly and Boudaoud (2008). Because we assume that the energy of the substrate is independent of $u(x)$ we can use the strain energy of the film (13) to solve the variational problem and from $\delta_{u(x)}\mathcal{E}_f = 0$ obtain $u'(x) + w'(x)^2/2 = \sum_{n=1}^{\infty} A_n^2 k_n^2/4$. Inserting $u(x)$ and $w(x)$ into Eq. (13) after integration yields

$$\mathcal{E}_f = \sum_{n=1}^{\infty}\left(\frac{C}{2}\left(\varepsilon_g^2 - \frac{\varepsilon_g k_n^2 A_n^2}{2} + \frac{1}{16}\sum_m^n k_m^2 A_m^2 k_{n-m}^2 A_{n-m}^2\right) + \frac{1}{4}Dk_n^4 A_n^2\right). \tag{14}$$

The total strain energy of the substrate can be formulated from the response of the substrate we use, the standard linear solid, also known as the Zener model (Christensen, 1982b). The corresponding shear modulus in the Laplace space can be written as

follows

$$\hat{\mu}(s) = \frac{\mu_{\text{neq}}}{s} + \frac{\mu_{\text{eq}}}{s + 1/\tau}. \tag{15}$$

Here, s is the Laplace transform parameter and $\hat{(\dots)} = \mathcal{L}\left((\dots)\right)_{(s)} = \int_{-\infty}^{\infty}(\dots)e^{-st}dt$ denotes the Laplace transformed variable. It follows that the stress in the incompressible substrate (for which $\varepsilon_{ij} = \varepsilon_{ij}^{\text{dev}}$) can be written as $\hat{\sigma}_{ij}(s) = 2\hat{\mu}_{\text{s}}(s)\, s\, \hat{\varepsilon}_{ij}(s) - \hat{p}\,\delta_{ij}/s$ or according to Christensen (1982b) in the time domain as

$$\sigma_{ij}(t) = \dot{\mu}_{\text{s}}(t) * \varepsilon_{ij}(t) - p\,\delta_{ij} = \int_{-\infty}^{t} \frac{d\mu_{\text{s}}(\bar{t})}{d\bar{t}} \varepsilon_{ij}(t-\bar{t})\, d\bar{t} \; - \; p\,\delta_{ij}. \tag{16}$$

Here, the symbol $*$ is used for the time convolution. Due to the incompressibility assumption, the hydrostatic pressure p does not cause any volumetric deformation and is therefore not needed to express the strain energy of the system. Another assumption in the substrate is that there is no horizontal displacements $u = 0$ and therefore also the σ_{xx} component does not contribute to the strain energy. We therefore only need the relationship between the deviatoric stresses σ_{xy} and σ_{yy} at the surface of the substrate and the normal displacement of the substrate for a certain harmonic load with a wave number k. According to Audoly and Boudaoud (2008) it can be written as:

$$\begin{pmatrix} \tilde{\sigma}_{xy}^{\text{dev}}(k,t) \\ \tilde{\sigma}_{yy}^{\text{dev}}(k,t) \end{pmatrix} = \frac{1}{(3-4\nu_{\text{s}})} \begin{pmatrix} \text{i}\,(1-2\nu_{\text{s}})\,k \\ 2\,(1-\nu_{\text{s}})\,k \end{pmatrix} \dot{\mu}_{\text{s}}(t) * A(k,t). \tag{17}$$

Here, $A_n(t) = A(k_n, t)$ and $\tilde{(\dots)} = \mathcal{F}\left(\dots\right)_{(k)} = \int_{-\infty}^{\infty}(\dots)\cos kx\; dx$ denote a Fourier-transformed variable. Because we assume that the substrate is incompressible and its response is linear, the average energy of the substrate per unit length with multiple deformation modes can, according to Parseval's theorem (Arfken et al., 2013), be written as

$$\mathcal{E}_{\text{s}}(t) = \frac{1}{2}\dot{E}_{\text{s}}^{*}(t) * \sum_{n=0}^{\infty} A(k_n,t)^2 k_n, \tag{18}$$

where $\dot{E}_{\text{s}}^{*}(t) = 2(1-\nu_{\text{s}})/(3-4\nu_{\text{s}})\;\dot{\mu}_{\text{s}}(t)$. The total average energy of the whole structure is a sum of the substrate's energy given in Eq. (18) and that of the film given by Eq. (14):

$$\mathcal{E} = \sum_{n=0}^{\infty}\left(\frac{C}{2}\left(\varepsilon_{\text{g}}^2 - \frac{\varepsilon_{\text{g}} k_n^2 A_n^2}{2} + \frac{1}{16}\sum_{m=0}^{n} k_m^2 A_m^2 k_{n-m}^2 A_{n-m}^2\right) + \frac{1}{4}Dk_n^4 A_n^2 + \frac{1}{2}\dot{E}_{\text{s}}^{*}(t) * A_n^2 k_n\right). \tag{19}$$

To obtain the equilibrium equations we study the first variation of the energy, $A_n(t)$ to obtain $\delta_{A_n(t)}\mathcal{E} = 0$ for all n,

$$C\left(-\frac{\varepsilon_{\text{g}} k_n^2 A_n}{2} + \frac{1}{16}\left(k_n^2 A_n \sum_{l=0}^{\infty} k_l^2 A_l^2 + k_n^4 A_n^3\right)\right) + \frac{1}{2}Dk_n^4 A_n + \dot{E}_{\text{s}}^{*}(t) * A_n k_n = 0. \tag{20}$$

We use the Laplace transform and insert Eq. (15) into Eq. (20) to obtain

$$\mathcal{L}\left(C\left(-\frac{\varepsilon_{\text{g}} k_n^2 A_n}{2} + \frac{1}{16}\left(k_n^2 A_n \sum_{l=0}^{\infty} k_l^2 A_l^2 + k_n^4 A_n^3\right)\right)\right)_{(s)} + \frac{1}{2}Dk_n^4 \mathcal{L}\left(A_n\right)_{(s)} + \left(E_{\text{s,eq}}^{*} + \frac{E_{\text{s,neq}}^{*}}{1+1/(\tau s)}\right)\mathcal{L}\left(A_n\right)_{(s)} k_n = 0. \tag{21}$$

We now multiply the whole equation by $(1+1/(\tau s))$, insert the Laplace transform relation $s = \mathcal{L}\left(\dot{(\dots)}(t)\right)_{(s)}/\mathcal{L}\left((\dots)(t)\right)_{(s)}$, perform an inverse Laplace transform and obtain a system of coupled deformation-mode, amplitude-evolution equations

$$\dot{A}_n(t) = -\frac{C\left(k_n \sum_{l=0}^{\infty} k_l^2 A_l^2 + k_n^3 A_n^2 - 8k_n\varepsilon_{\text{g}}(t)\right) + \left(16E_{\text{s,eq}}^{*} + 8Dk_n^3\right)}{C\left(k_n \sum_{l=0}^{\infty}\left(k_l^2 A_l^2 + 2k_l^2 A_l \dot{A}_l/\dot{A}_n\right) + 3k_n^3 A_n^2 - 8k_n\varepsilon_{\text{g}}(t)\right) + \left(16E_{\text{s,0}}^{*} + 8Dk_n^3\right)}\frac{A_n(t)}{\tau}, \tag{22}$$

which describe the amplitude development of the deformation pattern. In contrast to the work of Huang (2005), we formulated the substrate as in Audoly and Boudaoud (2008), where we implemented a viscoelastic material model. Therefore, the results are more consistent with our VH theory. Additionally, our set of equations is coupled through the nonlinear components $C\left(k_n \sum_{l=0}^{\infty} k_l^2 A_l^2 + k_n^3 A_n^2\right)$ and $C\left(k_n \sum_{l=0}^{\infty}\left(k_l^2 A_l^2 + 2k_l^2 A_l \dot{A}_l/\dot{A}_n\right) + 3k_n^3 A_n^2\right)$. These components describe the film's membrane stress relaxation due to the out-of-plane wrinkling and enable an analysis of the deformation evolution also in the post-buckling regime. From Eq. (22) it is clear that an increase in the amplitudes of the wrinkle-deformation modes $A_m(t)$, results in the damping of the out-of-plane wrinkling-amplitude growth rate $\dot{A}_n(t)$. Generally, the evolution of these multiple deformation modes is simultaneous, while one deformation mode is always energetically favorable and therefore develops the fastest. If the difference between the immediate μ_{s}^{0} and the equilibrium substrate shear modulus μ_{s}^{∞} is large enough then the spectrum of developing deformation modes is wide, and the favorable deformation mode with the largest growth rate $\dot{A}_n(t)$ changes with time, which means that the deformation mode with the leading amplitude $A_n(t)$ changes with time as well. This transition between the leading deformation modes is observed and analyzed in Figs. 6 and 8.

To explore the fundamentals of the deformation's evolution we can reduce our theory in two ways, both of which decouple the deformation modes in Eq. (22). (A) The first way is to only model structures where the substrate's immediate μ_{s}^{0} and equilibrium response μ_{s}^{∞} are similar, while the load ε_{g} is small enough. That way only one deformation mode n develops in the structure from the start to the static equilibrium, as will be shown later. With this reduction of the theory a closed-form solution can be obtained,

even though the system is still nonlinear and thus valid for moderate post-buckling deformations. (B) The second way is to linearize the system of Eq. (22), which is coupled only in the nonlinear terms. The onset of wrinkling of the whole spectrum of deformation modes can be determined and the fastest can be identified, but at the cost of being unable to simulate the post-buckling behavior and the competition between the deformation modes. Doing this and using a step function for loading, a theory similar to that of Huang (2005) can be recovered.

(A) Evolution of a single deformation mode

Let us assume that the immediate μ_s^0 and equilibrium response of the substrate μ_s^∞ are similar and that the load and the load rate are small enough, such that the wrinkle deformation patterns of the elastic theory in these limits have the same wavelength and therefore present bounds for the emerging deformation pattern wavelength. Because of that, we can expect that only one deformation mode amplitude A_n has positive growth rate and develops during the evolution of the pattern as the system of Eq. (22). The mode grows according to the expression for the evolution

$$\dot{A}_n(t) = -\frac{C\left(A_n^2(t)k_n^3 - 4k_n\varepsilon_g(t)\right) + \left(8E^*_{s,eq} + 4Dk_n^3\right)}{C\left(3A_n^2(t)k_n^3 - 4k_n\varepsilon_g(t)\right) + \left(8E^*_{s,0} + 4Dk_n^3\right)}\,\frac{A_n(t)}{\tau}, \tag{23}$$

where n indicates the number of wrinkles in the deformation mode, and the absence of the summation indicates that only one deformation mode is present in the structure.

Since we assume that only one deformation mode with n wrinkles develops and remains in the structure, we only need to find which one has the fastest rate of amplitude increase at the start of the wrinkling. If we consider $k_n = k(n)$ as a continuous variable and $\dot{A}_n(t) = \dot{A}(t,k)$ as a continuous distribution of the amplitude growth rate, then the leading (and the only) deformation mode in the structure can be sought by finding the deformation mode with the fastest growth rate $\dot{A}_{\text{fastest}}(t,k)$, by finding the extremal value of k by $d\dot{A}(t,k)/dk = 0$. At the start of the wrinkling in the limit $\lim_{t\to 0} A(t) = 0$ (and after that because of the assumption of only one deformation mode) this yields

$$k_{\text{fastest}} = \frac{2}{h_f}\sqrt{\varepsilon_g(t)}. \tag{24}$$

It is interesting to note that the fastest-growing deformation mode does not depend on the structure's material properties, but only on the growth strain function $\varepsilon_g(t)$ and the film thickness h_f. If the growth strain function is limited to the step function $\varepsilon_g(t) = \bar{\varepsilon}_g$, the result of Huang (2005): $k_{\text{fastest}} = 2\sqrt{\bar{\varepsilon}_g}/h_f$ would be recovered, where the fastest deformation mode is not directly dependent on the time. It only depends on time through the time-dependent amplitude change, which is not considered in the form of Eq. (24) because of the assumption $\lim_{t\to 0} A(t) = 0$. In the case when the loading is a ramp function $\varepsilon_g(t) = \dot{\varepsilon}_g t$, the dominant deformation pattern also explicitly changes with the time during the deformation pattern's evolution $k_{\text{fastest}} = 2\sqrt{\dot{\varepsilon}_g t}/h_f$ and not only indirectly through the time-dependent amplitude change, which, again, is not considered in Eq. (24).

The deformation mode k_{fastest} is the fastest-growing mode, but might not be attainable due to the boundary conditions that enable only deformation modes $k = k_n = 2\pi n/L$, where $n \in \{0.5, 1, 1.5, \ldots\}$. Thus, we search for the fastest-growing mode by choosing the deformation mode closest to k_{fastest} that is attainable and has the largest growth rate $\dot{A}_n$. When $\mu_s^0 \gtrsim \mu_s^\infty$, we find that this dominant deformation mode is constant through the whole evolution of deformations, which makes it possible to evaluate the whole deformation evolution of the wrinkling pattern from the evolution Eq. (23).

With the use of our reduced theory from Eqs. (23) and (24) we can analyze the wrinkling of the system with one deformation mode for a ramp function and in the limit as $\dot{\varepsilon}_g \to \infty$ for a step function. In this limit we recover the findings of Huang (2005), but only qualitatively since a different model of the substrate was used. For the sake of completeness, we present the results below. In addition to Huang (2005), we also show the deformation mode's evolution in the post-buckling regime and validate it using our fully nonlinear VH model (see Section 3).

(A.1) Evolution of a single deformation mode due to ramp loading

With a known deformation mode k_n at hand and the mode evolution Eq. (23), we plot the phase space $(t, \dot{A}_n(t))$ and the streamlines $(1, \dot{A}_n(t))$ for a ramp loading in Fig. 4a. The differential Eq. (23) has two limits, depicted with blue curves: the top represents the equilibrium limit curve, while the bottom represents a pole limit curve. In the equilibrium limit curve's deformation the growth rate is zero $\dot{A}_n(t) = 0$ (zero of the numerator in Eq. (23)),

$$A_{n,\text{eq}}(t) = \sqrt{\frac{4Ck_n\varepsilon_g(t) - 8E^*_{s,\text{eq}} - Dk_n^3}{Ck_n^3}}, \tag{25}$$

while the second limit curve $A_{n,\text{p}}$ corresponds to the subspace of the phase space, where the amplitude growth rate of the deformation mode is infinite $\dot{A}_n(t) \to \infty$ (zero of the denominator in Eq. (23)), which yields the pole curve of the phase space

$$A_{n,\text{p}}(t) = \sqrt{\frac{4Ck_n\varepsilon_g(t) - 8E^*_{s,0} - Dk_n^3}{3Ck_n^3}}. \tag{26}$$

To obtain the transient solution for the ramp loading, Eq. (23) has to be solved numerically. As observed in Fig. 4 (pink, red and orange curves with $\dot{\varepsilon}_g/(1/\tau) \in \{0.0002, 0.0004, 0.0008\}$) the wrinkle amplitude enters the unstable (non-equilibrium) region of the phase space between the two limits and after passing $t_{\infty,\text{cr}}$ (defined as $A_{n,\text{eq}}(t_{\infty,\text{cr}}) = 0$) rapidly diverges from the unwrinkled trivial

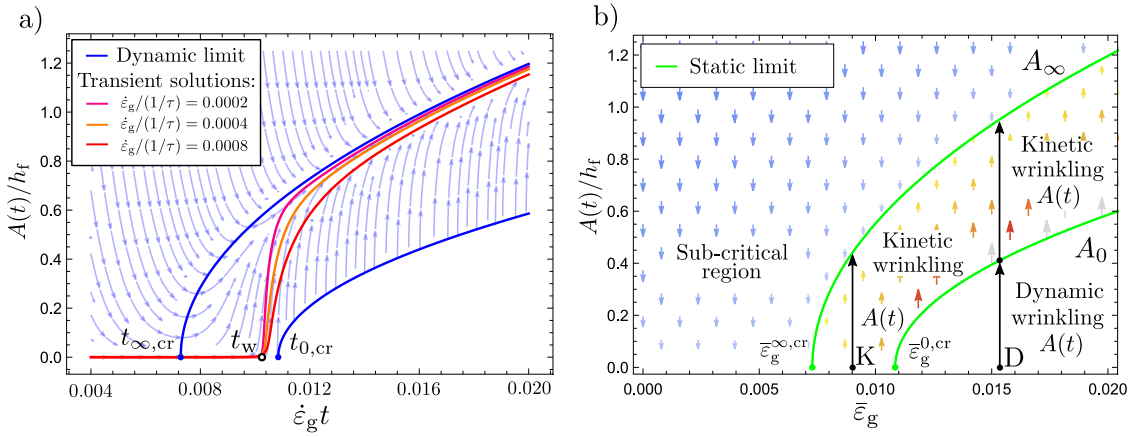

Fig. 4. Response of the structure in the toy model with only one deformation mode. (a) Phase portrait of the kinetic evolution of the normalized wrinkle amplitude $A(t)/h_f$ in time t for a leading deformation mode with $k_{fastest}$ as the structure is subjected to ramp loading. Blue curves represent limit solutions corresponding to zeros of the numerator and denominator of Eq. (23) describing the wrinkle evolution, i.e., the $t \to \infty$ solution (on the left) and the pole of the streamline field for $t \to 0$ (on the right), respectively. The transient solutions $A(t)$ (pink, red and orange curves) correspond to different ratios between the viscoelastic substrate stress relaxation times and the growth rate $\dot{\varepsilon}_g/(1/\tau) \in \{0.0002, 0.0004, 0.0008\}$. In all cases $\dot{\varepsilon}_g = 0.004$ 1/s. The streamlines represent the time gradient of the wrinkle amplitude and time vector $(1, A'(t)/h_f) = (dt/dt, d(A(t)/h_f)/dt)$ in $(t, A(t)/h_f)$ phase space. (b) Phase portrait of the evolution of the normalized wrinkle amplitude $A(t)/h_f$ as a function of the growth strain amplitude $\bar{\varepsilon}_g$ for a leading deformation mode $k_{fastest}$ for step loading (a limit case, when $\dot{\varepsilon}_g \to \infty$). Three distinct growth mechanisms can be identified according to Huang (2005); (*i*) sub-critical growth: when the growth strain $\bar{\varepsilon}_g$ is smaller than the equilibrium critical growth strain $\bar{\varepsilon}_g < \varepsilon_{crit,\infty}$ – in this case all the initial deformation modes decay; (*ii*) kinetic wrinkle growth: when the growth strain $\bar{\varepsilon}_g$ is larger than the equilibrium critical growth strain and smaller than the immediate critical growth strain, i.e., $\varepsilon_{crit,\infty} < \bar{\varepsilon}_g < \varepsilon_{crit,0}$ – in this regime the deformation modes due to the initial imperfections start to grow exponentially with time to A_∞ amplitude; (*iii*) dynamic wrinkle growth: when growth strain $\bar{\varepsilon}_g$ is larger than the immediate critical growth strain $\bar{\varepsilon}_g > \varepsilon_{crit,0}$ – here the wrinkles grow immediately (dynamically) to the A_0 amplitude and then kinetically to the A_∞ amplitude.

equilibrium state at point t_w (defined as $0 < A_n(t_w) \ll A_{n,eq}(t_w)$), which cannot be later than at $A_{n,0}(t_{0,cr}) = 0$. This transient-solution curve then diverges from the limit-pole solution and approaches to the dynamic equilibrium limit solution in Eq. (25).

(A.2) Evolution of a single deformation mode due to step loading

We subject the structure in the toy model to a step loading function of growth that enables us to observe the deformation pattern's evolution in the post-buckling regime. This kind of loading and deformation pattern's evolution was already analyzed by Huang; however, only qualitatively in Im and Huang (2005) due to the use of a different substrate theory and in the immediate post-buckling regime in Huang (2005), due to the use of the linearized theory. With our toy model we are able to reproduce his qualitative results, where he discovered three distinct wrinkle-growth phases, which are shown in Fig. 4(a), and we repeat here for the sake of completeness:

(*i*) sub-critical growth: when the growth strain $\bar{\varepsilon}_g$ is smaller than the equilibrium critical growth strain $\bar{\varepsilon}_g < \varepsilon_{crit,\infty}$. In this case all the initial deformation modes due to any kinds of disturbances decay.

(*ii*) kinetic wrinkle growth: when the growth strain $\bar{\varepsilon}_g$ is larger than the equilibrium critical growth strain and smaller than the immediate critical growth strain $\varepsilon_{crit,\infty} < \bar{\varepsilon}_g < \varepsilon_{crit,0}$. In this regime deformation modes due to initial imperfections start to grow exponentially with time to the A_∞ amplitude from the first Eq. in (27);

(*iii*) dynamic wrinkle growth: when growth strain $\bar{\varepsilon}_g$ is larger than the immediate critical growth strain $\bar{\varepsilon}_g > \varepsilon_{crit,0}$. The wrinkles grow immediately (dynamically) to the A_0 amplitude and then kinetically to the A_∞ amplitude from the Eq. (27).

Furthermore, we extend the analysis of Huang (2005) to moderate post-buckling with the use of our moderately nonlinear toy model in this subsection.

Because the step-loading function is the limit case of a limited ramp function as $\dot{\varepsilon}_g \to \infty$, we can also use Eq. (23) to model the structure's behavior and compute the leading deformation mode k_n from Eq. (24). Its phase space $(\bar{\varepsilon}_g, A_n(t))$ and its time gradient $(0, \dot{A}_n(t))$ are presented in Fig. 4(b). Similar to the dynamic limits in Eqs. (26) and (25), we can find the static limits of the theory from Eq. (23) by considering no viscoelastic relaxation with $\tau \to \infty$ and an immediate viscoelastic relaxation with $\tau \to 0$ and obtain the static solutions as

$$A_{n,\infty} = h_f\sqrt{\bar{\varepsilon}_g/\varepsilon_{\infty,cr} - 1}, \quad \text{where} \quad \varepsilon_{\infty,cr} = \frac{1}{4}\left(\frac{4\left(1-\nu_f^2\right)\left(1-\nu_s\right)}{\left(1+\nu_s\right)\left(3-4\nu_s\right)}\frac{3E_{s,\infty}}{E_f}\right)^{2/3}$$
$$A_{n,0} = h_f\sqrt{\bar{\varepsilon}_g/\varepsilon_{0,cr} - 1}, \quad \text{where} \quad \varepsilon_{0,cr} = \frac{1}{4}\left(\frac{4\left(1-\nu_f^2\right)\left(1-\nu_s\right)}{\left(1+\nu_s\right)\left(3-4\nu_s\right)}\frac{3E_{s,0}}{E_f}\right)^{2/3}. \tag{27}$$

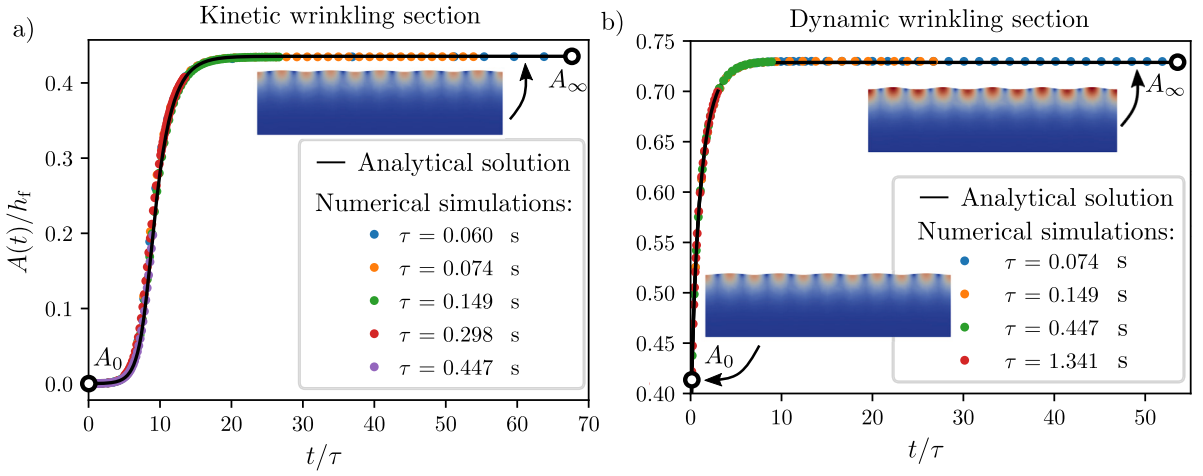

Fig. 5. Growth of the normalized wrinkle-deformation mode amplitude $A(t)/h_f$ due to step loading as a function of normalized time t/τ and viscoelastic stress relaxation in the substrate for one deformation mode due to $\mu_s^0 \gtrsim \mu_s^\infty$ for the deformation mode $n = 5$. (a) Kinetic phase corresponding to section K in Fig. 4(b) for stress relaxation times $\tau \in \{0.060, 0.074, 0.149, 0.298, 0.447\}$ s and $\bar{\varepsilon}_g = 0.10$. (b) Dynamic (immediate) phase followed by the kinetic phase corresponding to section D in Fig. 4(b) for the stress relaxation times $\tau \in \{0.074, 0.149, 0.447, 1.341\}$ s and $\bar{\varepsilon}_g = 0.14$. In both cases, colored dots represent numerical (FEM) solutions according to the continuous visco-hyperelastic theory for different stress-relaxation times τ, while the solid black line represents the analytical solution of the toy model. The material and geometric parameters are as follows: $\mu_s^0/\mu_s^\infty = 8$, $\mu_s^0 = 3.859 \times 10^{-3}\mu_f$, $\mu_f = E_f/(2(1-\nu_f^2))$, where μ_s^0 and μ_s^∞ are the immediate and equilibrium shear moduli of the substrate, μ_f and $E_f = 1.0$ MPa are the shear and Young's moduli of the film, $\nu_f = \nu_s = \nu = 0.49$ is the Poisson's ratio of the film and the substrate, while $h_f = 1.2$ mm and $H = 59.0$ mm are the thicknesses of the film and the substrate, respectively. The length of the structure is $L = 200.0$ mm.

Furthermore, the relationship between the amplitude of the wrinkles $A_n(t)$ and the normalized time t/τ between these time limits is, with our nonlinear theory, obtained by solving Eq. (23) for the step loading and can be written as

$$t/\tau = \frac{K_1\left(\log A_n(t) - \log A_{n,0}\right) - 12E^*_{s,neq}\left(1-\nu_f^2\right)\left(\log K_2(A_n(t)) - \log K_2\left(A_{n,0}\right)\right)}{\left(E_f h_f k_n\left(-h_f^2 k_n^2 + 12\bar{\varepsilon}_g\right) - 24E^*_{s,e}\left(1-\nu_f^2\right)\right)}, \tag{28}$$

where

$$K_1 = E_f h_f k_n\left(h_f^2 k_n^2 - 12\bar{\varepsilon}_g\right) + 24\left(E^*_{s,eq} + E^*_{s,neq}\right)\left(1-\nu_s^2\right),$$
$$K_2(A) = E_f h_f k_n\left(3A^2 k_n^2 + h_f^2 k_n^2 - 12\bar{\varepsilon}_g\right).$$

The amplitude growth in the kinetic regime is a sigmoid function that at the beginning grows exponentially from the initial imperfection amplitude A_0 (the start of the sigmoid function) and then approaches the equilibrium amplitude A_∞ asymptotically (end of the sigmoid function). On the other hand, in the dynamic regime the amplitude already has some finite magnitude A_0, and then it approaches the equilibrium amplitude A_∞ (the end part of the sigmoid function). Both these cases are shown in Section 3, in Fig. 5a and (b).

(B) Onset of wrinkling

To analyze the start of the wrinkling growth for potentially more than one deformation mode that develop simultaneously, we linearize the evolution Eq. (22) around the undeformed configuration, which causes uncoupling of the equations around the limit $A_n(t) \to 0$. It is shown that each mode grows according to the following expression

$$\dot{A}_n(t) = -\frac{Ck_n\varepsilon_g(t) - \left(2E^*_{s,eq} + Dk_n^3\right)}{Ck_n\varepsilon_g(t) - \left(2E^*_{s,0} + Dk_n^3\right)}\frac{A_n(t)}{\tau}, \tag{29}$$

for all n. In contrast to the reduction in (A), where we limited the parameters so that only one mode could exist, there exists here a set of k_n, for which the amplitude growth rate is positive, $\dot{A}_n(t) > 0$, and the initial amplitudes $A_{n,0}$ due to material imperfections grow, and a set of k_n, where $\dot{A}_n(t) < 0$ for which the initial imperfections decay (for detailed description see Huang, 2005). In the case when $\mu_s^0 \gg \mu_s^\infty$ a whole spectrum of deformation modes will start to grow exponentially and compete with each other. If the difference between μ_s^0 and μ_s^∞ is small, then the range of k_n with a positive growth rate $\dot{A}_n(t)$ is narrow or even only one deformation mode has a positive growth rate. To find the fastest-growing deformation mode, we use the same method as for the solution of Eq. (24).

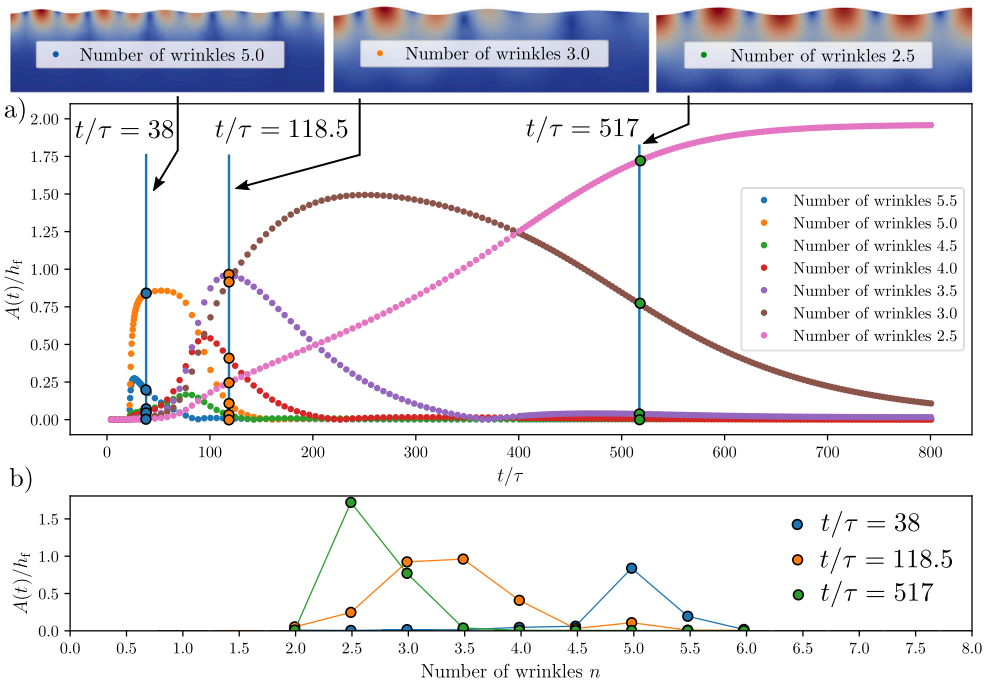

Fig. 6. Multiple-wrinkle-mode evolution due to step loading as a function of normalized time t/τ and viscoelastic stress relaxation in the substrate. a) Normalized wrinkle amplitudes $A(t)/h_f$ of different deformation modes with $n \in \{2.5, 3, 3.5, 4, 4.5, 5, 5.5\}$ number of wrinkles obtained numerically from the visco-hyperelastic continuum model, plotted as a function of normalized time t/τ. On the top $n = 5$, $n = 3$ and $n = 2.5$ deformation modes at $t/\tau = 38$, 118.5, 517 are shown, respectively. The amplitudes of the deformation modes are extracted using a discrete Fourier transform of the vertical displacements from the centerline of the film. To also obtain the half modes, the domain is mirrored before the discrete Fourier transform is carried out. (b) Amplitude distributions $A(t)/h_f$ of different deformation modes are given for the same particular values of t/τ as in panel a. Among the competing modes, the system has one dominant mode at the beginning and at the end, while more competing modes can be observed at the intermediate time. The parameters in this simulation were: $\mu_s^0/\mu_s^\infty = 27$, $\mu_s^\infty = 1.429 \times 10^{-4}\mu_f$, viscoelastic stress-relaxation constant $\tau = 0.05$ s, while other parameters are the same as in Fig. 5a.

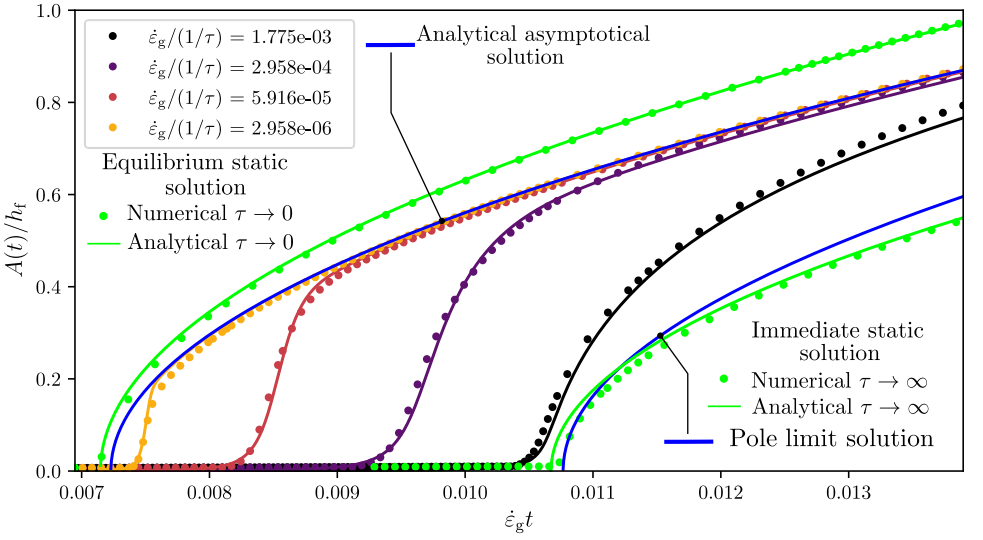

Fig. 7. Comparison between the dominant deformation-mode solutions of the toy model and the visco-hyperelastic model in terms of normalized wrinkle amplitude $A(t)/h_f$ as a function of normalized time $\dot{\varepsilon}_g t = \varepsilon_g$ for different normalized substrate stress-relaxation times $\dot{\varepsilon}_g/(1/\tau) \in \{1.775 \times 10^{-3}, 2.958 \times 10^{-4}, 5.916 \times 10^{-5}, 2.958 \times 10^{-6}\}$ when the structure is subjected to a ramp loading with $\dot{\varepsilon}_g = 0.004$ and only one deformation mode is present due to the choice of parameters. Dots represent numerical results based on the continuum visco-elastic model discussed in Section 2.1, while solid lines represent numerical solutions of the toy model discussed in Section 2.3 in Eq. (23). Two dynamic limit cases, representing asymptotic and pole solutions, can be obtained analytically for the toy model (given with blue solid lines), see Eq. (25). Moreover, an analytical solution can also be obtained for the two static limits represented with solid green lines, see Eq. (27). In both cases the structure acts as purely elastic with the immediate substrate shear modulus μ_s^0 at $\tau \to \infty$ (left curve) and μ_s^∞ at $\tau \to 0$ (right curve). The parameters of the system are chosen such that the dominant wrinkle wavelength of the structure does not change during the evolution of the deformation and they are the same as in Fig. 5.

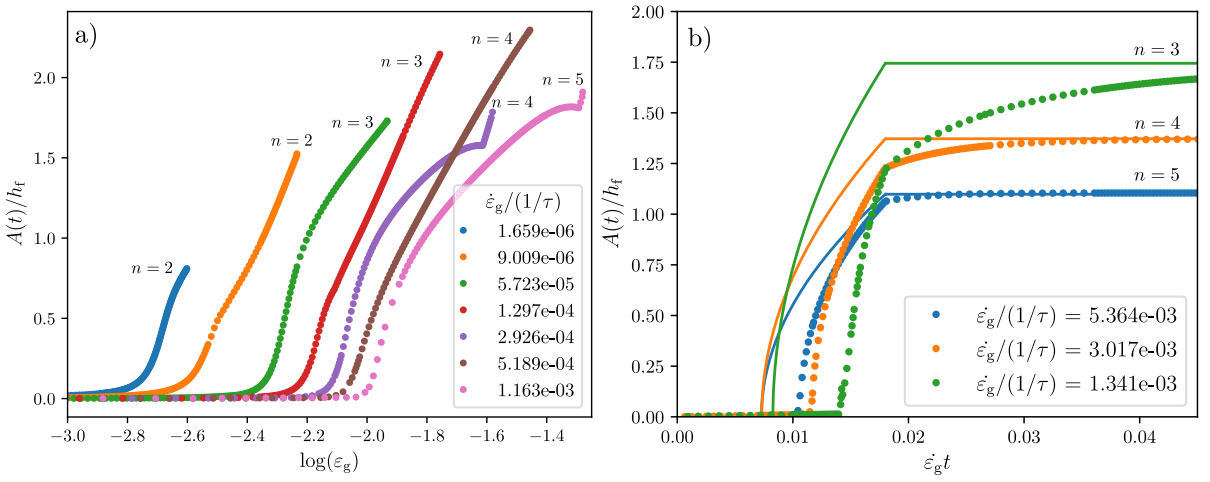

Fig. 8. Influence of different ratios between the loading rates of the film and the viscoelastic stress-relaxation rates of the substrate $\dot{\varepsilon}_g/(1/\tau)$ on the (main) leading deformation mode when the structure is subjected to limited ramp loading. (a) Normalized wrinkling amplitude $A(t)/h_f$ of the dominant mode as a function of horizontal film-growth strain ε_g at (different) $\dot{\varepsilon}_g/(1/\tau)$. The material and geometric parameters are the same as in Fig. 6. (b) Normalized wrinkle amplitude $A(t)/h_f$ of the dominant deformation mode as a function of normalized time $\dot{\varepsilon}_g t$ for different $\dot{\varepsilon}_g/(1/\tau)$. Colored dots represent a numerical solution of the VH model and solid lines represent the dynamic asymptotic limits of these solutions, towards which the structure is developing. The dynamic asymptotic limits are calculated from the toy model (see Eq. (25)). The film-growth strain-limited ramp function $\dot{\varepsilon}_g(t)$ is defined as in Eq. (11) and has the parameters $t_0 = 0$, $\dot{\varepsilon}_g = 0.009$ 1/s and $\bar{\varepsilon}_g = 0.018$, while other parameters are the same as in Fig. 6.

(B.1) Onset of wrinkling due to ramp loading

The solution of the linearized and decoupled system of Eq. (29) for the ramp loading $\varepsilon_g(t) = \dot{\varepsilon}_g t$ is

$$A_n(t) = A_{n,0} e^{-t/\tau} \left(Dk_n^3 + 2E^*_{s,0}\right)^{\frac{2(E^*_{s,0}-E^*_{s,eq})}{Ck_n\dot{\varepsilon}_g\tau}} \left(\frac{1}{Dk_n^3 + 2E^*_{s,0} - Ck_n\dot{\varepsilon}_g t}\right)^{\frac{2(E^*_{s,0}-E^*_{s,eq})}{Ck_n\dot{\varepsilon}_g\tau}}. \tag{30}$$

This formula only applies for small amplitudes A_n and times before the pole point $t_p = \left(Dk_n^3 + 2E^*_{s,0}\right)/\left(Jk_n\dot{\varepsilon}_g\right)$, when the denominator reaches 0. Since nonlinear solutions of the decoupled system are available, Fig. 4a (red, orange and pink lines), the solution of the linearized system is not shown. We see that the amplitudes of the deformation modes are very small for a long time (near $A_{n,0}$), but start to grow extremely fast near the point t_w, which can be defined as the time when the wrinkle amplitude starts to grow rapidly, but is still much smaller than the dynamic equilibrium amplitude given by Eq. (25): $0 < A(t_w) \ll A_{n,eq}(t_w)$. This point t_w depends on the pole point of the linearized solution t_p, the ratio between the growth rate and the viscoelastic substrate stress relaxation rate $\dot{\varepsilon}_g/(1/\tau)$ (contained in the exponent in the solution) and on the initial amplitude of the deformation mode $A_{n,0}$.

In the initial pattern evolution all of many initial deformation-mode amplitudes $A_{n,0}$ with $\dot{A}_n(t) > 0$ have a tendency to develop in the structure until one of the deformation modes is large enough to damp the development of the other deformation modes. Therefore, which deformation mode will develop in the structure mainly depends on three parameters: (1) the initial imperfection spectrum $A_{n,0}$, (2) the rate of growth strain $\dot{\varepsilon}_g$ and (3) the viscoelastic stress-relaxation constant τ. For (1), this means that $k_{fastest}(t)$ at the beginning of the loading is small in structures subjected to a ramp-function loading, see Eq. (24). Therefore, if the initial imperfections have large amplitudes $A_{n,0}$, one of the deformation modes A_n will soon, still at small $k_{fastest}(t)$, reach an amplitude that will cause the damping of all the other deformation modes and the deformation mode with a small number of wrinkles will develop. For (2), this means that the deformation modes with a small number of wrinkles will be preferable for a longer time in structures for which the growth strain rate $\dot{\varepsilon}_g$ is small, see Eq. (24), and the developing deformation modes will have fewer wrinkles. Moreover, wrinkling will occur at a smaller growth strain, because the viscoelastic substrate reacts as being less stiff to slower deformation rates. For (3), this means that if the viscoelastic stress-relaxation constant of the substrate τ is small, then the substrate will act as less stiff and the deformation patterns with a smaller number of wrinkles will be promoted and will develop in the structure.

All of this is applicable in the early stages of the wrinkling-pattern development, while later when the deformation modes have grown to some finite amplitude, other modes might develop and the dominant deformation mode might change. This occurs when the difference between the immediate μ_s^0 and the equilibrium shear modulus of the substrate μ_s^∞ is large enough to allow for many different, favorable deformation modes. In that case the growth rate of the dominant deformation mode $\dot{A}_k(t)$ also depends on the current amplitude spectrum of the other deformation modes $A_k(t)$, see Eq. (22).

(B.2) Onset of wrinkling due to step loading

In the case of step loading $\varepsilon_g(t) = \bar{\varepsilon}_g$ we qualitatively recover the results by Huang (2005), who considered the response of the substrate with the use of a different, less accurate substrate model. Here, we observe how the structure develops towards

the static final equilibrium configuration in the kinetic wrinkle-development phase. The structure is undeformed at the start and many deformation modes start to grow/decay (depending on the parameters) independently and exponentially. The solutions of the linearized Eq. (29) are

$$A_n(t) = A_{n,0} \exp\left(-\frac{Ck_n\bar{\varepsilon}_g - \left(2E^*_{s,eq} + Dk_n^3\right)}{Ck_n\bar{\varepsilon}_g - \left(2E^*_{s,0} + Dk_n^3\right)} \frac{t}{\tau} \right), \tag{31}$$

where $A_{n,0}$ are the amplitudes of the deformation modes of the initial imperfection in the structure. The amplitudes of the deformation modes $A_n(t)$ grow exponentially with time at first (as the Eq. (31) indicates), but then start to asymptotically approach the final equilibrium amplitudes A_∞, which is not considered by this linearized solution but is by the system of Eq. (8). If only one deformation mode develops in the structure, then this A_∞ corresponds to the solution from the Eq. (28), also shown in Fig. 4(b) marked as A_∞.

3. Results and discussion

In this section we present the deformation pattern's evolution due to a horizontal growth strain ε_g in the film for the analyzed structure subjected to loading with step and ramp time functions. The results are obtained numerically by solving the fully nonlinear VH theory (the details can be found in Appendix) and analytically/semi-analytically by solving the toy model (22) with the use of the 4th-order Runge–Kutta integrator in Mathematica. The VH theory is solved for the vertically free and horizontally fixed displacements and fixed rotations of the film and the substrate on the left- and right-hand sides of the domain. This boundary conditions only allow the deformation modes $n \in \{0.5, 1, 1.5, 2, 2.5, \dots\}$ in the system. To model the system past the bifurcation point, we use a small vertical perturbation force on the left-hand side of the film with the magnitude $E_f h_f/1000$, which excites all the deformation modes equally since $\mathcal{F}(\delta(x))_{(k)} = 1$. In both the step- and ramp-loading cases, we first present the deformation pattern's evolution on a bi-layer with rather similar immediate and equilibrium shear moduli $\mu_s^0 \gtrsim \mu_s^\infty$, which causes the development of only one deformation mode. Then we present cases where $\mu_s^0 \gg \mu_s^\infty$ and a whole spectrum of deformation modes develops, whereby the deformation evolution's time is greatly increased due to the multistability and the transition between the deformation modes. In the case of ramp loading, we observe that the final equilibrium-deformation mode depends on the transient time parameters (growth rate and viscoelastic relaxation rate).

3.1. Step loading

We first analyze a structure with the material and geometrical characteristics given in Fig. 5. This structure is subjected to step-growth strain $\varepsilon_g(t) = \bar{\varepsilon}_g$, which has similar immediate and equilibrium moduli of the substrate $\mu_s^0 \gtrsim \mu_s^\infty$ and therefore deforms with only a single deformation mode. We compare the normalized wrinkle amplitudes $A_n(t)/h_f$ of our toy model with the FE results of the VH model in the case of a step loading with a horizontal growth strain in the film ε_g for the kinetic and dynamic wrinkling phases with different values of the viscoelastic stress-relaxation constants τ of the substrate. In the kinetic wrinkle-growth phase in Fig. 5a (for reference see Fig. 4(b) at point K), the normalized amplitude of the wrinkles $A_n(t)/h_f$, first grows exponentially due to the exponential drop in the substrate's effective shear modulus $\mu_s(t)$, see Fig. 2(b). When $\mu_s(t)$ approaches the equilibrium effective shear modulus μ_s^∞ and the normal stresses caused by film growth in the film relax due to the out-of-plane deformation of the film, the normalized deformation mode's amplitude $A_n(t)/h_f$ asymptotically approaches the equilibrium deformed configuration. In the dynamic wrinkle-growth phase in Fig. 5(b) (for reference see Fig. 4(b) at point D) the amplitude of wrinkles first grows immediately (dynamically) to the initial $A_{n,0}$ amplitude as if the substrate was elastic with the shear modulus μ_s^∞. When the effective shear modulus of the substrate decays and the normal stresses due to film growth relax through the out-of-plane film deformation, the normalized deformation-mode amplitude $A_n(t)/h_f$ asymptotically approaches the equilibrium amplitude A_∞/h_f. In both cases, because the viscoelastic stress-relaxation constant of the substrate τ is the only time constant of the structure, the numerical (colored dots) and analytical (black line) results for the different τ merge into one line if we normalize the time with τ. This normalization can be seen from the analytical solution in Eq. (28). We also observe that the time in which the toy model structure reaches equilibrium is around $(10–20)\tau$, while the time of the stress relaxation of the homogeneously uniaxially strained structure is around 4τ. This is because the normal stresses due to a constrained horizontal film growth also relax through the out-of-plane wrinkling, which then drive the deformation processes much more slowly.

Furthermore, we analyze a similar structure subjected to horizontal growth strain in a film in the shape of a step function $\varepsilon_g(t) = \bar{\varepsilon}_g$ in a kinetic wrinkle-growth regime, but this time the immediate and equilibrium shear moduli of the structure are very different ($\mu_s^0 \gg \mu_s^\infty$), so that multiple deformation modes evolve and compete from the start of the wrinkling to the equilibrium configuration, where one dominant mode prevails. Fig. 6a shows the evolution of multiple, normalized, competing deformation-mode amplitudes $A_n(t)/h_f$ from the FE analysis of the structure. Multiple, competing deformation modes in the structure develop due to the fact that the viscoelastic substrate relaxes with time and therefore different deformation modes develop at different rates through the deformation pattern's evolution. The first few dominant deformation modes that grow in the structure are with $n = 5$ and $n = 5.5$ wrinkles, due to the still relatively large effective stiffness of the substrate. This amplitude spectrum can also be observed in Fig. 6b in blue, which shows a relatively narrow amplitude distribution at the start with $t/\tau = 38$. When the effective stiffness of the substrate reduces, the deformation pattern changes (orange dots and lines at $t/\tau = 118.5$). Higher deformation modes decay and a wider amplitude spectrum emerges. Towards the end of the evolution cycle (green dots and lines at $t/\tau = 517$) also the middle-range

deformation modes decay and the lower deformation modes (with $n = (3-2.5)$) are expressed due to the softening of the substrate. In the end, only the deformation mode with $n = 2.5$ wrinkles remains. We observe that the time of this deformation pattern's evolution is much longer ($\sim 700\,\tau$) than the material's stress-relaxation time ($\sim 4\tau$), or the deformation pattern's evolution of the structure with only one deformation mode (see Fig. 5), where it was around $\sim 15\tau$. This is due to the emergence of multiple out-of-plane wrinkling–deformation modes at the start of the wrinkling that relax the normal stresses due to the horizontal film growth. Because these normal stresses are relaxed and because the differences in the strain energy of the different wrinkling–deformation modes is relatively small, the structure does not have a lot of energy that is readily available to be dissipated for a rapid deformation transition.

3.2. Ramp loading

Next, we analyze the structure subjected to the ramp loading. In the case when the choice of material parameters does not allow for multiple deformation modes in the structure ($\mu_s^0 \gtrsim \mu_s^\infty$), a single deformation mode develops, which was schematically presented in Fig. 4a. Fig. 7 shows normalized amplitudes $A(t)/h_f$ for $\dot{\varepsilon}_g/(1/\tau) \in \{1.775\times10^{-3}, 2.958\times10^{-4}, 5.916\times10^{-5}, 2.958\times10^{-6}\}$ and $\tau \in \{0, \infty\}$ obtained from both models: the fully nonlinear VH model, solved with FE analysis (colored dots), and solutions obtained from the toy model (colored lines). A remarkably good agreement can be observed. We notice that a shorter viscoelastic stress-relaxation time τ of the substrate causes a smaller resistance to wrinkling. Therefore, such structure wrinkles into the equilibrium (asymptotic wrinkle amplitude $A(t)/h_f$) faster than the structure with a longer viscoelastic stress-relaxation time τ. We also see that if we set $\tau \to \infty$ in the numerical simulation the substrate never relaxes the stresses and we obtain a result similar to that of the elastic system with an immediate (non-equilibrium) shear modulus of the substrate μ_s^0. Similarly, if we set $\tau \to 0$ in the numerical simulation, the substrate relaxes immediately and we obtain a result similar to that of the elastic system with an equilibrium shear modulus of the substrate μ_s^∞.

In contrast to the previous example with similar immediate and equilibrium responses of the substrate ($\mu_s^0 \gtrsim \mu_s^\infty$), very different material parameters ($\mu_s^0 \gg \mu_s^\infty$) promote the occurrence of multiple deformation modes, which are also influenced by different ramp strain rates $\dot{\varepsilon}_g$ (i.e., different ratios $\dot{\varepsilon}_g/(1/\tau)$). Fig. 8a shows the evolution of the leading deformation modes that correspond to modes with the largest amplitude $A(t)/h_f$ in the structure with the same material and geometric parameters as given in the caption of Fig. 6. The faster strain rates $\dot{\varepsilon}_g$ induce deformation modes with a larger number of wrinkles, because the viscoelastic substrate responds as being stiffer to faster loads. The deformation pattern that evolves in the structure maximizes the release of the film's membrane energy ($\sim An^2$), and at the same time minimizes both the film's bending ($\sim An^4$) and the substrate's stretching energies ($\sim An$). The deformation patterns with low n minimize the bending energy ($\sim An^4$); however, they require large amplitudes to release enough membrane energy from the film ($\sim An^2$), which means they cause large substrate energy ($\sim An$) and are therefore not energetically favorable. On the other hand, deformation patterns with large n release a larger amount of membrane energy $\sim An^2$ at low amplitudes, but the film stores a lot of bending energy ($\sim An^4$), which is also not energetically favorable. Therefore, the system chooses a deformation mode with a moderate n, which releases a moderate amount of membrane energy from the film and at the same time does not store a large amount of bending energy in the film, nor stretching energy in the substrate. The increase in the substrate's resistance to deformation (effective stiffness) due to higher deformation rates $\dot{\varepsilon}_g$ causes greater influence of the substrate in the energy balance and the structure develops a deformation pattern with a larger number of wrinkles n.

Next, we analyze the equilibrium deformation state of the systems loaded with different loading-rate/viscoelastic stress-relaxation ratios $\dot{\varepsilon}_g/(1/\tau)$. While in structures that behave as linearly viscoelastic, these ratios only affect the transient response and not the equilibrium modes, surprisingly, the ratio also affects the final equilibrium state of our nonlinear system. We observed that the ratio between the growth rates and the viscoelastic stress-relaxation rates in the substrate $\dot{\varepsilon}_g/(1/\tau)$ affects not only the choice of the transient deformation mode, but also the final equilibrium deformation mode (number of wrinkles n) in the structure. This can be observed in Fig. 8b, where the evolution of the largest deformation mode's normalized amplitudes $A(t)/h_f$, obtained from the VH theory and FE analysis, are shown. The structures with geometric and material parameters as in Fig. 6, but with different $\dot{\varepsilon}_g/(1/\tau)$ ratios, are subjected to a limited-ramp-load function $\varepsilon_g(t)$ and due to the different $\dot{\varepsilon}_g/(1/\tau)$ ratios, different deformation patterns start to develop in the structure. Because our structure permits moderately large deformations, which cause (i) a nonlinear response of the film and (ii) a nonlinear response (neo-Hookean material model) of the substrate, there are multiple, locally stable, final equilibrium-deformation states. Due to the different transient viscoelastic properties of the structures in Fig. 8, the three structures develop to three different locally stable final equilibrium deformation states, also called "frozen" deformation states.

To further explore the occurrence of the locally stable "frozen" deformation states we analyze the evolution of the transient-deformation-normalized amplitude spectrum (due to different $\varepsilon_g/(1/\tau)$ ratio) in Fig. 9a and c. The normalized amplitudes $A(t)/h_f$ are computed for the structure that is modeled with the continuum visco-hyperelastic (VH) theory for two different $\dot{\varepsilon}_g/(1/\tau) \in \{0.0003352, 0.0020115\}$ and with the same growth-strain function and parameters as in Fig. 8b. Due to the nonlinearity, completely different deformation amplitudes develop and evolve to different equilibrium configurations. Note that this was not the case in our toy model, as shown in Fig. 9b and d, even though we used the same parameters. The difference can, therefore, be primarily attributed to the model of the substrate, which was a linear (Saint Venant-Kirchhoff) viscoelastic material model in the toy model. In both cases in Fig. 9b and d the deformation pattern evolves in roughly the same way, but on a different time scale. Moreover, the deformation pattern evolves towards the final deformation mode with $n = 5$ wrinkles in the structure, similarly as in the case 9c, and in contrast to the case in Fig. 9a, where the deformation mode with $n = 4$ decays early and the deformation mode with $n = 4.5$ evolves in the structure.

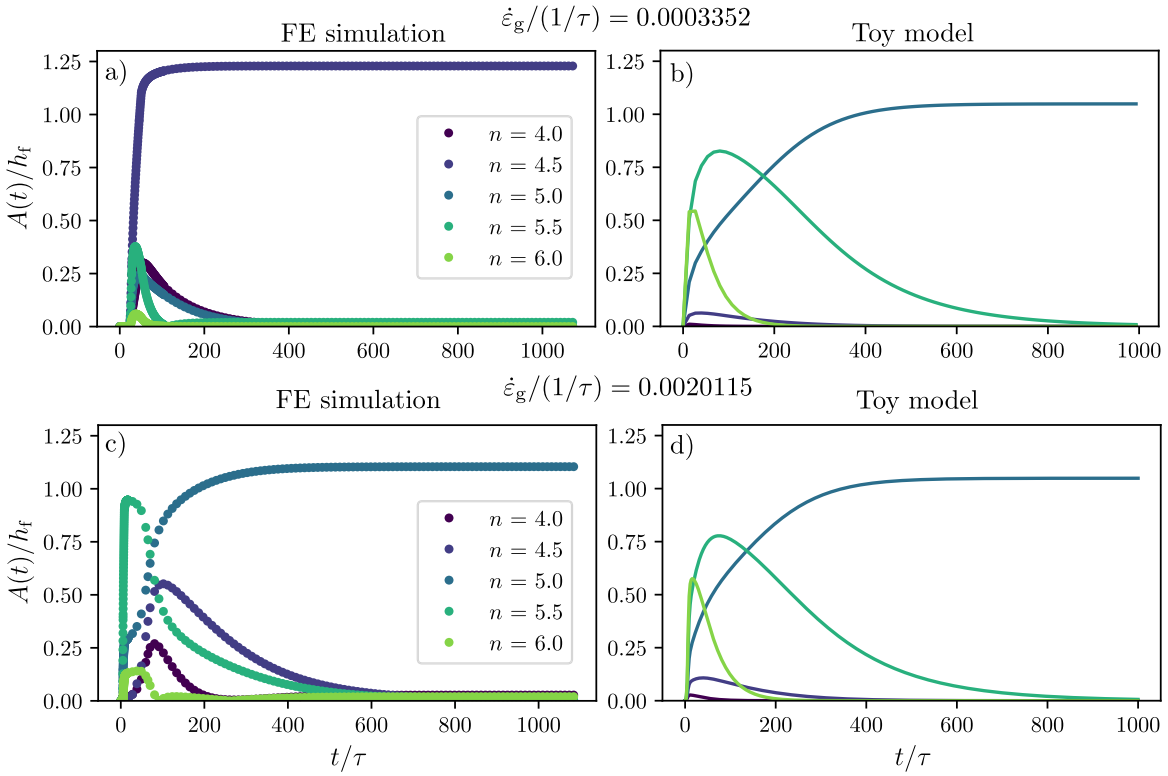

Fig. 9. Normalized deformation-mode amplitudes $A(t)/h_f$ as a function of normalized time $\dot{\varepsilon}_g t$ for a limited ramp function at short and long stress viscoelastic relaxation times τ. Solutions for $\dot{\varepsilon}_g/(1/\tau) = 0.00033525$ obtained by (a) FE simulations, based on the continuum VH theory, and for (b) numerical solution of the toy model (22), reveal that many deformation modes develop simultaneously at the start, but quickly decay. In the case of FE simulations only the $n = 4.5$ mode (purple dots) remains at the end, while in the toy model this initially dominant mode (green line) also begins to decay and the $n = 5.0$ mode takes over (blue line), at approximately $t/\tau = 200$. Solutions for $\dot{\varepsilon}_g/(1/\tau) = 0.0020115$ obtained by (c) FE simulations, show that even more deformation modes develop simultaneously and compete at the start. Over time only the deformation mode with $n = 5.0$ wrinkles (green line) survives, and the solutions of the toy model (d) show qualitatively similar results in which also only $n = 5.0$ mode survives. The discrepancy between the VH numerical simulation and the toy model is due to the consideration of the nonlinear response of the substrate in the VH simulation, while the toy model only considers a linear response of the substrate. The parameters of the limited ramp function were $t_0 = 0$, $\dot{\epsilon}_g = 0.009$ 1/s and $\bar{\varepsilon}_g = 0.018$, while the other parameters are the same as in Fig. 6. The legend in panel (a) applies to all the panels.

4. Conclusion

We have developed a finite-deformation visco-hyperelastic theoretical model, which is based on the standard linear solid and the neo-Hookean solid. The core of the model relies on the multiplicative decomposition of finite deformations into parts due to loading, non-equilibrium elasticity and viscosity. The theory can be used for modeling general viscoelastic structures subjected to arbitrary time-dependent loads. To study the coupling effects of multistability of (quasi-)periodic deformation patterns and viscoelasticity, we focused on the wrinkling of a thin elastic film attached to a viscoelastic substrate under plane-strain assumptions. The structure was subjected to a spatially constrained, time-dependent, homogeneous growth in the direction of the film's mid-surface. The problem was solved numerically using the finite-element method and the dynamic relaxation method. In parallel, we developed a reduced-order model to comb the parametric space of the problem more easily. The reduced model considered the thin elastic film as a Föppl–von Karman plate and the substrate was reduced to linear viscoelastic. With these approximations, we were able to find closed-form solutions for dynamic and static wrinkling limits for ramp- and step-time-function growth, the evolution of deformation patterns for the step-time-function growth with exactly one dominant mode and linearized evolution equations for all the growth cases. The transient evolution equations were all solved numerically. Both developed theoretical models, i.e., the visco-hyperelastic and the reduced, assumed growth of the elastic film as a ramp, limited ramp and step-time function in the direction of the film's mid-surface.

For growth as a step-time function two distinct cases with an approximately equal substrate rigidity $\mu_s^0 \gtrsim \mu_s^\infty$ and significantly different substrate rigidities $\mu_s^0 \gg \mu_s^\infty$ were considered. Numerical solutions obtained via FE simulations on the visco-hyperelastic model revealed that when $\mu_s^0 \gtrsim \mu_s^\infty$, only one deformation mode is dominant, even far into the post-buckling region and throughout the entire evolution in time. The results agreed very well with our analytical predictions based on the reduced-order model. Furthermore, with linearization of our analytical model we recovered a solution, similar to that of Huang (2005), who characterized the kinetic and dynamic wrinkling phases. We showed that in this case ($\mu_s^0 \gtrsim \mu_s^\infty$ and step-growth functions), even far into the

nonlinear post-buckling region, the viscoelastic stress-relaxation time τ is the only parameter that scales the deformation evolution timescale of a single deformation mode and does not influence the wrinkling amplitude or the type of deformation mode that develops in the system. We found that the timescale of the deformation evolution in the kinetic/dynamic phase can be much longer than the timescale of viscoelastic relaxation of the material itself (e.g. up to 4 times longer for the selected case) even with only one deformation mode growing in the structure. A significantly different response of the structure is observed when $\mu_s^0 \gg \mu_s^\infty$. From the numerical FE simulations of the visco-hyperelastic model we observe a high level of competition between the multiple wrinkling modes in the nonlinear regime. Modes with more wrinkles develop first, but are eventually replaced by modes with fewer wrinkles as the stresses in the substrate relax. The timescale of the evolution is even larger (e.g., up to 200 times for the selected case) due to film's out-of-plane deformation, which releases a large part of the strain energy in the wrinkling process. This slows down the rate of viscoelastic relaxation and the deformation evolution. We hypothesize that, if the environmental variables (e.g., polymerization or phase transition) changed during this long transition, the structure would become "frozen" in a seemingly non-equilibrium deformation state, which is unattainable with a purely elastic structure.

Similar to the step-time-function growth, two distinct cases with an approximately equal substrate rigidity $\mu_s^0 \gtrsim \mu_s^\infty$ and significantly different rigidities $\mu_s^0 \gg \mu_s^\infty$ were considered for the ramp-time-function growth. Both of our models again predict that when $\mu_s^0 \gtrsim \mu_s^\infty$, only one deformation mode develops in the structure, but two phases can be identified during the deformation evolution: a fast, transient wrinkle-development phase at the start of the wrinkling and a slower, dynamic equilibrium wrinkle-development phase — which could be considered as a generalization of the two wrinkle-growth phases (kinetic and dynamic) from the step-loading case. In contrast to the step-loading example, in the ramp-loading example when $\mu_s^0 \gg \mu_s^\infty$, the film's growth rate $\dot{\epsilon}_g$ influences the wrinkling–deformation rate and because the reaction of the viscoelastic substrate is strain-rate dependent, $\dot{\epsilon}_g$ affects the timescale of the evolution, the choice of the transient deformation mode and even to which of the many final equilibrium deformation states the structure will evolve. A faster growth strain $\dot{\epsilon}_g$ encourages the development of a pattern with more wrinkles, which changes during the relaxation of the substrate. While the number of wrinkles gradually reduces, still more of them remain compared to the step-loading case. From the perspective of step loading this can be regarded as a pattern that is "frozen" in a seemingly non-equilibrium configuration. However, this phenomenon is not visible in our reduced model, where the substrate is modeled as linear viscoelastic. Therefore, we attribute this response in the structure to material nonlinearity and/or the coupling of the material's nonlinearity with the viscoelasticity.

Multiple available, final equilibrium-deformation states are generally the result of nonlinearities and not the transient viscoelastic behavior. However, in systems such as wrinkled elastic films on viscoelastic substrates, where many final deformation states are possible, it is not easy to predict to which final deformation state the system will evolve, especially without considering the full viscoelastic deformation pattern's evolution, as shown in this paper. We have shown that the coupling of multi-stability and viscoelasticity leads to locking of the system in a seemingly non-equilibrium deformation pattern that is unavailable for a purely elastic system and leads to a significant increase in the time of the transient deformation pattern's evolution, because the strain energy is also released through the loss of stability due to wrinkling. In other words, the slower deformation evolution of the structure is a consequence of less available energy in the system, which drives the viscoelastic dissipation and deformation evolution, for the energy was also released through wrinkling instability.

The results of this study will allow for a more comprehensive and rigorous mechanistic description of some biological processes such as morphogenesis, where viscoelasticity in conjunction with multi-stability plays an important role, e.g., lung (Goodwin et al., 2019), brain (Tallinen et al., 2016) and intestine (Shyer et al., 2013). In addition it will enable the engineering of structures that exploit the coupling of multi-stability with viscoelasticity for advanced functionalities connected with an increase in rigidity with the rate of loading, such as for ballistic protection, smart speed bumps, and the combined dissipative effects of viscoelasticity and the instabilities in applications such as vibration and sound insulation, and shock absorption.

CRediT authorship contribution statement

Jan Zavodnik: Conceptualization, Methodology, Software, Formal analysis, Computations, Investigation, Writing – original draft, Writing – review & editing. **Andrej Košmrlj:** Conceptualization, Methodology, Investigation, Resources, Writing – review & editing, Supervision. **Miha Brojan:** Conceptualization, Methodology, Investigation, Resources, Writing – review & editing, Supervision, Project administration, Funding acquisition.

Declaration of competing interest

The authors declare that they have no known competing financial interests or personal relationships that could have appeared to influence the work reported in this paper.

Data availability

Data will be made available on request.

Acknowledgment

Authors gratefully acknowledge the financial support of the Slovenian Research Agency (project grant numbers J2-9223 and J2-2499).

Appendix. Techniques used in the FEM

(Plane strain assumption) The deformation pattern's evolution in uniaxially growing elastic films on a planar viscoelastic substrate is analyzed using plane-strain assumptions. Our general visco-hyperelastic (VH) theory is thus reduced to plane strains, simply by enforcing $\partial()/\partial X_3 = 0$ and $u_3 = const$. Therefore, the stress equilibrium Eq. $(8)_1$ need to be solved in only 2 directions for 2 components of displacements $\boldsymbol{u}$ instead of 3. Similarly, only 3 evolution equations from Eq. $(8)_2$ need to be solved for the internal variable $\mathbf{C}_v$ with 3 different components, instead of 6 in a general 3D case.

(Finite element formulation) An open-source FE Computational Software (FEniCS Logg et al., 2011; Alnæs et al., 2015) is used to discretize the displacement field $\boldsymbol{u}$ and viscous-strain field $\mathbf{C}_v$ to transform the nonlinear system of PDEs in (8) to a system of nonlinear algebraic Eqs. The software is capable of the automatic differentiation of PDEs, FE discretization, mesh generation and solving the generated nonlinear system of equations with the use of the Newton–Raphson method. Our rectangular domain of width L and height H displayed in Fig. 3 was divided into the film and the substrate subdomains. They were meshed using triangular unstructured mesh, which was denser near the film. Based on the convergence analysis it was found that 1000 triangular, mixed finite elements were sufficient avoid volumetric locking of the elements in nearly incompressible solids, Logg et al. (2011), Alnæs et al. (2015) and Yu and Netherton (2000) with the Poisson's ratios $\nu_{eq} = \nu_{neq} = 0.49$. The mixed finite elements were composed of a 3rd-degree Lagrange finite element for the nodal displacements $\boldsymbol{u}$ and a 3rd-degree discrete Lagrange finite element for the internal variables $\mathbf{C}_v$.

(Temporal discretization) Implicit backward-step temporal discretization was used because of its numerical stability and because it allows larger time steps than the forward-stepping schemes (Hrapko et al., 2006; Prevost et al., 2011; Bilston et al., 2001; Reese and Govindjee, 1998; Carniel and Fancello, 2017). The time derivative was discretized as $\dot{(\,)} = \left((\,)_{n+1} - (\,)_n\right)/\Delta t$.

(Numerical algorithms for solving the nonlinear systems of equations) The spatial FE and temporal implicit Euler discretization provide a system of nonlinear algebraic equations to be solved. The solution process is started from an initial condition, where the system is first loaded by the perturbation force described in Section 3. Then the time stepping is initiated, where for each step an iterative process is employed to find the equilibrium configuration of the current time step. In the iterative process a Newton–Raphson iteration is employed, due to its efficiency. In cases when the tangent matrix is nearly singular due to instability, the dynamic relaxation method described in Oakley and Knight (1995) and Joldes et al. (2011a) is employed, because of its robustness and stability.

References

Allen, H.G., 1969. Analysis and Design of Structural Sandwich Panels. Pergamon, New York.

Alnæs, M., Blechta, J., Hake, J., Johansson, A., Kehlet, B., Logg, A., Richardson, C., Ring, J., Rognes, M., Wells, G., 2015. The FEniCS project version 1.5. 3, http://dx.doi.org/10.11588/ans.2015.100.20553.

Arfken, G., Weber, H., Harris, F., 2013. Mathematical Methods for Physicists: A Comprehensive Guide. Elsevier Science, URL https://books.google.si/books?id=qLFo_Z-PoGIC.

Audoly, B., Boudaoud, A., 2008. Buckling of a stiff film bound to a compliant substrate—Part I:: Formulation, linear stability of cylindrical patterns, secondary bifurcations. J. Mech. Phys. Solids 56 (7), 2401–2421. http://dx.doi.org/10.1016/j.jmps.2008.03.003.

Balbi, V., Kuhl, E., Ciarletta, P., 2015. Morphoelastic control of gastro-intestinal organogenesis: Theoretical predictions and numerical insights. J. Mech. Phys. Solids 78, http://dx.doi.org/10.1016/j.jmps.2015.02.016.

Ben Amar, M., Goriely, A., 2005. Growth and instability in elastic tissues. J. Mech. Phys. Solids 53, 2284–2319. http://dx.doi.org/10.1016/j.jmps.2005.04.008.

Berthier, L., Kurchan, J., 2013. Nonequilibrium glass transitions in driven and active matter. Nat. Phys. 9, http://dx.doi.org/10.1038/nphys2592.

Bilston, L., Liu, Z., Phan-Thien, N., 2001. Large strain behaviour of brain tissue in shear: Some experimental data and differential constitutive model. Biorheology 38, 335–345.

Brau, F., Damman, P., Diamant, H., Witten, T., 2013. Wrinkle to fold transition: Influence of the substrate response. Soft Matter 9, 8177–8186. http://dx.doi.org/10.1039/c3sm50655j.

Budday, S., Sommer, G., Holzapfel, G., Steinmann, P., Kuhl, E., 2017. Viscoelastic parameter identification of human brain tissue. J. Mech. Behav. Biomed. Mater. 74, 463–476. http://dx.doi.org/10.1016/j.jmbbm.2017.07.014, URL http://www.sciencedirect.com/science/article/pii/S1751616117303004.

Budday, S., Steinmann, P., Kuhl, E., 2014. The role of mechanics during brain development. J. Mech. Phys. Solids 72, http://dx.doi.org/10.1016/j.jmps.2014.07.010.

Cao, Y., Hutchinson, J.W., 2012. Wrinkling phenomena in neo-hookean film/substrate bilayers. J. Appl. Mech. 79 (3), http://dx.doi.org/10.1115/1.4005960, arXiv:https://asmedigitalcollection.asme.org/appliedmechanics/article-pdf/79/3/031019/5689626/031019_1.pdf. 031019.

Carniel, T.A., Fancello, E.A., 2017. Modeling the local viscoelastic behavior of living cells under nanoindentation tests. Latin Am. J. Solids Struct. 14, 844–860.

Chen, X., Hutchinson, J.W., 2004. Herringbone buckling patterns of compressed thin films on compliant substrates. J. Appl. Mech. 71 (5), 597–603. http://dx.doi.org/10.1115/1.1756141, arXiv:https://asmedigitalcollection.asme.org/appliedmechanics/article-pdf/71/5/597/5471575/597_1.pdf.

Christensen, R., 1982a. Preface to First Edition, second ed. Academic Press, pp. xi–xii. http://dx.doi.org/10.1016/B978-0-12-174252-2.50004-1, URL http://www.sciencedirect.com/science/article/pii/B9780121742522500041,

Christensen, R., 1982b. Chapter I - Viscoelastic stress strain constitutive relations. In: Christensen, R. (Ed.), Theory of Viscoelasticity, second ed. Academic Press, pp. 1–34. http://dx.doi.org/10.1016/B978-0-12-174252-2.50005-3.

Goodwin, K., Mao, S., Guyomar, T., Miller, E., Radisky, D.C., Košmrlj, A., Nelson, C.M., 2019. Smooth muscle differentiation shapes domain branches during mouse lung development. Development 146 (22), http://dx.doi.org/10.1242/dev.181172, URL https://dev.biologists.org/content/146/22/dev181172.arXiv:https://dev.biologists.org/content/146/22/dev181172.full.pdf.

Goriely, A., Ben Amar, M., 2007. On the definition and modeling of incremental, cumulative, and continuous growth laws in morphoelasticity. Biomech. Model. Mechanobiol. 6, 289–296. http://dx.doi.org/10.1007/s10237-006-0065-7.

Harris, A.R., Peter, L., Bellis, J., Baum, B., Kabla, A.J., Charras, G.T., 2012. Characterizing the mechanics of cultured cell monolayers. Proc. Natl. Acad. Sci. 109 (41), 16449–16454. http://dx.doi.org/10.1073/pnas.1213301109, URL https://www.pnas.org/content/109/41/16449. arXiv:https://www.pnas.org/content/109/41/16449.full.pdf.

Hoger, A., 1997. Virtual configurations and constitutive equations for residually stressed bodies with material symmetry. J. Elasticity 48, 125–144. http://dx.doi.org/10.1023/A:1007459331524.

Hrapko, M., Van Dommelen, J., Peters, G., Wismans, J., 2006. The mechanical behavior of brain tissue: Large strain response and constitutive modeling. Biorheology 43, 623–636.
Huang, R., 2002. Wrinkling of a compressed elastic film on a viscous layer. J. Mech. Phys. Solids 91, 1135–1142. http://dx.doi.org/10.1063/1.1427407.
Huang, R., 2005. Kinetic wrinkling of an elastic film on a viscoelastic substrate. J. Mech. Phys. Solids 53, 63. http://dx.doi.org/10.1016/j.jmps.2004.06.007.
Huang, Z., Hong, W., Suo, Z., 2005. Nonlinear analyses of wrinkles in a film bonded to a compliant substrate. J. Mech. Phys. Solids 53, 2101–2118. http://dx.doi.org/10.1016/j.jmps.2005.03.007.
Hutchinson, J.W., 2013. The role of nonlinear substrate elasticity in the wrinkling of thin films. Phil. Trans. R. Soc. A 371 (1993), 20120422. http://dx.doi.org/10.1098/rsta.2012.0422, URL https://royalsocietypublishing.org/doi/abs/10.1098/rsta.2012.0422. arXiv:https://royalsocietypublishing.org/doi/pdf/10.1098/rsta.2012.0422.
Im, S.H., Huang, R., 2005. Evolution of wrinkles in elastic-viscoelastic bilayer thin films. J. Appl. Mech. 72 (6), 955–961. http://dx.doi.org/10.1115/1.2043191, arXiv:https://asmedigitalcollection.asme.org/appliedmechanics/article-pdf/72/6/955/5472832/955_1.pdf.
Im, S., Huang, R., 2008. Wrinkle patterns of anisotropic crystal films on viscoelastic substrates. J. Mech. Phys. Solids 56 (12), 3315–3330. http://dx.doi.org/10.1016/J.JMPS.2008.09.011.
Joldes, G., Wittek, A., Miller, K., 2011a. An adaptive Dynamic Relaxation method for solving nonlinear finite element problems. Application to brain shift estimation. Int. J. Numer. Methods Biomed. Eng. 27, 173–185. http://dx.doi.org/10.1002/cnm.1407.
Joldes, G.R., Wittek, A., Miller, K., 2011b. An adaptive dynamic relaxation method for solving nonlinear finite element problems. Application to brain shift estimation. Int. J. Numer. Methods Biomed. Eng. 27 (2), 173–185. http://dx.doi.org/10.1002/cnm.1407, URL https://onlinelibrary.wiley.com/doi/abs/10.1002/cnm.1407. arXiv:https://onlinelibrary.wiley.com/doi/pdf/10.1002/cnm.1407.
Kawasaki, H., Mouri, T., 2019. Humanoid robot hand and its applied research. J. Mechatron. Robotics 31 (1), 16–26. http://dx.doi.org/10.20965/jrm.2019.p0016.
Lifshitz, E., Kosevich, A., Pitaevskii, L., 1986. Chapter II - the equilibrium of rods and plates. In: Lifshitz, E., Kosevich, A., Pitaevskii, L. (Eds.), Theory of Elasticity, third ed. Butterworth-Heinemann, Oxford, pp. 38–86. http://dx.doi.org/10.1016/B978-0-08-057069-3.50009-7, URL https://www.sciencedirect.com/science/article/pii/B9780080570693500097.
Lin, P., Vajpayee, S., Jagota, A., Hui, C.Y., Yang, S., 2008. Mechanically tunable dry adhesive from wrinkled elastomers. Soft Matter 4, 1830–1835. http://dx.doi.org/10.1039/B802848F.
Logg, A., Wells, G., Mardal, K.-A., 2011. Automated solution of differential equations by the finite element method. The FEniCS Book. vol. 84, http://dx.doi.org/10.1007/978-3-642-23099-8,
Lubarda, V., Hoger, A., 2002. On the mechanics of solids with a growing mass. Int. J. Solids Struct. 39 (18), 4627–4664. http://dx.doi.org/10.1016/S0020-7683(02)00352-9.
Matoz-Fernandez, D.A., Agoritsas, E., Barrat, J.-L., Bertin, E., Martens, K., 2017. Nonlinear rheology in a model biological tissue. Phys. Rev. Lett. 118, 158105. http://dx.doi.org/10.1103/PhysRevLett.118.158105, URL https://link.aps.org/doi/10.1103/PhysRevLett.118.158105.
Matoz-Fernandez, D.A., Davidson, F.A., Stanley-Wall, N.R., Sknepnek, R., 2020. Wrinkle patterns in active viscoelastic thin sheets. Phys. Rev. Res. 2, 013165. http://dx.doi.org/10.1103/PhysRevResearch.2.013165, URL https://link.aps.org/doi/10.1103/PhysRevResearch.2.013165.
McRae, O., Oratis, A.T., Bird, J.C., 2021. Viscous wrinkling of nonuniform sheets. Phys. Rev. Fluids 6, 110506. http://dx.doi.org/10.1103/PhysRevFluids.6.110506, URL https://link.aps.org/doi/10.1103/PhysRevFluids.6.110506.
Oakley, D.R., Knight, N.F., 1995. Adaptive dynamic relaxation algorithm for non-linear hyperelastic structures Part I. Formulation. Comput. Methods Appl. Mech. Engrg. 126 (1), 67–89. http://dx.doi.org/10.1016/0045-7825(95)00805-B, URL https://www.sciencedirect.com/science/article/pii/004578259500805B.
Ogden, R., 2013. Non-Linear Elastic Deformations. In: Dover Civil and Mechanical Engineering, Dover Publications, URL https://books.google.si/books?id=52XDAgAAQBAJ.
Pocivavsek, L., Dellsy, R., Kern-Goldberger, A., Johnson, S., Lin, B., Lee, K.Y., Cerda, E., 2008. Stress and fold localization in thin elastic membranes. Science 320 (5878), 912–916. http://dx.doi.org/10.1126/science.115406.
Prevost, T.P., Balakrishnan, A., Suresh, S., Socrate, S., 2011. Biomechanics of brain tissue. Acta Biomater. 7 (1), 83–95. http://dx.doi.org/10.1016/j.actbio.2010.06.035.
Rauzi, M., Verant, P., Lecuit, T., Lenne, P.-F., 2008. Nature and anisotropy of cortical forces orienting Drosophila tissue morphogenesis. Nature Cell Biol. 10 (12), 1401–1410. http://dx.doi.org/10.1038/ncb1798, URL http://europepmc.org/abstract/MED/18978783.
Reese, S., Govindjee, S., 1998. A theory of finite viscoelasticity and numerical aspects. Int. J. Solids Struct. 35 (26), 3455–3482. http://dx.doi.org/10.1016/S0020-7683(97)00217-5, URL https://www.sciencedirect.com/science/article/pii/S0020768397002175.
de Rooij, R., Kuhl, E., 2017. A physical multifield model predicts the development of volume and structure in the human brain. J. Mech. Phys. Solids 112, http://dx.doi.org/10.1016/j.jmps.2017.12.011.
Sabbah, A., Youssef, A., Damman, P., 2016. Superhydrophobic surfaces created by elastic instability of PDMS. Appl. Sci. 6 (5), 1–8. http://dx.doi.org/10.3390/app6050152.
Shyer, A., Tallinen, T., Nerurkar, N., Wei, Z., Gil, E.S., Kaplan, D., Tabin, C., Mahadevan, L., 2013. Villification: How the gut gets its villi. Science 342 (6155), 212–218. http://dx.doi.org/10.1126/science.1238842.
Tallinen, T., Chung, J.Y., Rousseau, F., Girard, N., Lefevre, J., Mahadevan, L., 2016. On the growth and form of cortical convolutions. Nat. Phys. 12, 588–593. http://dx.doi.org/10.1038/NPHYS3632.
Timoshenko, S., Gere, J., 2012. Theory of Elastic Stability. In: Dover Civil and Mechanical Engineering, Dover Publications, URL https://books.google.si/books?id=98B6JOW2HiUC.
Truby, R., Wehner, M., Grosskopf, A., Vogt, D., Uzel, S., Wood, R., Lewis, J., 2018. Soft somatosensitive actuators via embedded 3D printing. Adv. Matter 30 (15), 1–8. http://dx.doi.org/10.1002/adma.201706383.
Yan, J., Fei, C., Mao, S., Moreau, A., Wingreen, N., Košmrlj, A., Stone, H., Bassler, B., 2019. Mechanical instability and interfacial energy drive biofilm morphogenesis. ELife 8, http://dx.doi.org/10.7554/eLife.43920.
Yavari, A., 2010. A geometric theory of growth mechanics. J. Nonlinear Sci. 20 (6), 781–830. http://dx.doi.org/10.1007/s00332-010-9073-y, URL http://dx.doi.org/10.1007/s00332-010-9073-y.
Yu, H.S., Netherton, M.D., 2000. Performance of displacement finite elements for modelling incompressible materials. Int. J. Numer. Anal. Methods Geomech. 24 (7), 627–653. http://dx.doi.org/10.1002/(SICI)1096-9853(200006)24:7<627::AID-NAG86>3.0.CO;2-L.